Synthesis and Characterization of Fe^{3+} doped $PbTiO_3$ Nanopowders

by

Kamil KiRAZ

A Thesis Submitted to the

Graduate School of Engineering

in Partial Fulfillment of the Requirements for

the Degree of

Master of Science

in

Material Science and Engineering

Koç University

April 2009

Koc University

Graduate School of Sciences and Engineering

This is to certify that I have examined this copy of a master's thesis by

Kamil KİRAZ

and have found that it is complete and satisfactory in all respects,
and that any and all revisions required by the final
examining committee have been made.

Committee Members:

Mehmet Suat Somer, Ph. D. (Advisor)

Uğur Ünal, Ph. D.

Murat Sözer, Ph. D.

Date: 27th of April, 2009

ABSTRACT

A set of Fe^{3+}- modified $PbTiO_3$ nanopowders which is a widely used ferro- and piezo-electric ceramic material has been synthesized according to the combined polymerization and pyrolysis (CPP) route of metallorganic precursors with subsequent calcination at various temperatures. This study aimed to shift the unit cell of $PbTiO_3$ crystals from tetragonal to cubic phase at room temperature by adjusting the optimum reaction time and temperature by doping 0,025 mole % $Fe^{3+}$and by ball milling the yield. Different reaction temperatures (300-900°C) are tried for the most efficient energy / grain size ratio.

In order to obtain $PbTiO_3$ crystals, an organo-metallic sol-gel precursor is used. By applying proper thermal treatment and synthesis route, grain size reduction is succeeded in the order of nanometers (10 – 400nm range). X-Ray Diffraction and Raman characterization are used to calculate the unit cell parameters, to confirm material identity and purity, as well as to verify the formation of a $PbTiO_3$ perovskitic phase and the existence of ferroelectricity.

Furthermore, the prevailing defect structure has been investigated by means of electron paramagnetic resonance (EPR) spectroscopy. The EPR results clearly indicate marked size effects by approaching to the critical grain size ($d_{crit} < 12$ nm) at which a size-driven tetragonal-to-cubic phase transition is observed at room temperature. As a function of mean grain size, either $(Fe_{Ti}^{'} - V_O^{\bullet\bullet})^{\bullet}$ defect dipoles or 'isolated' defects $Fe_{Ti}^{'}$ are formed. These results are analyzed in terms of a core-shell model. Accordingly, the obtained Fe^{3+}-modified $PbTiO_3$ nanoparticles consist of a ferroelectric core, a distorted interface region, and a cubic dead layer which is paraelectric.

ÖZET

Ferroelektrik ve piezoelektrik özellikleri ile bilinen bir seramik malzeme olan kurşun titanatın ($PbTiO_3$) eser miktarda Fe^{3+} karıştırılmış nano tozlarının sentezi ardışık polimerizasyon ve piroliz yöntemi ile farklı sıcaklıklarda gerçekleştirilmiştir. Çalışmanın ana amacı reaksiyon koşullarını optimize ederek oda sıcaklığında nano boyutta kübik kristal yapısını elde etmeye çalışmaktır. Bu esnada en az energy ile küçük parçacık boylarını elde etmek amaçlı, molar yüzdede %0,025 Fe^{3+} kullanılarak 300°C ila 900°C arasındaki sentez sıcaklıkları denenmiştir.

$PbTiO_3$ 'in sentezinde başlangıç malzemelesi olarak organometalik öncü hazırlanmıştır. Gerekli reaksiyon şartları sonrasında boyutları 10 nanometre ile 400 nanometre arasında çeşitli kristaller sentezlenmiştir. Ürün analizi için kullanılan karakterizasyon tekniklerinden XRD ve Raman karakterizasyonu sayesinde, kristal parametreleri hesaplanmış, ürün yapısı ve saflığı teyit edilmiş ve de ferroelektrik özellikte perovskit yapısında $PbTiO_3$ elde edildiği anlaşılmıştır.

Ayrıca, yapıdaki demirden kaynaklanan bozukluk elektron paramanyetik resonans tekniğiyle (EPR spektroskopisi) araştırılmıştır. Bu metotla yapının büyüklüğü kritik büyüklük olan ve tetragonal fazdan kübik faza geçişin olduğu 12 nanometreye doğru azaldıkça kristal yapısında oluşan etkiler gözlemlenmiştir. Yapının büyüklüğüne göre ya $(Fe_{Ti}^{'} - V_O^{\bullet\bullet})^{\bullet}$ defekt yapı dipolü ya da izole kusur olan $Fe_{Ti}^{'}$ bölgesi görülür. Bu sonuçlar çekirdek ve dış kabuk teorisi ile açıklanmaktadır. Bu teoriye göre, elde ettiğimiz Fe^{3+} ile karıştırılmış $PbTiO_3$ nanoparçacıkları ferroelektrik bir çekirdeğe, bozunmuş bir arayüze ve de en dışta paraelektrik olan pasif katman yapısına sahiptir.

ACKNOWLEDGEMENTS

I would like to thank,

- my supervisor and role model, Prof. Dr. Mehmet Suat Somer for his endless support, precious helps and for giving me the chance to be a part of his research team throughout the BS and MSc years,
- biricik ailemden sevgiliden sevgili integrallerim Ayşe ve Ahmet Kiraz çiftine, Ünal ve Şenol abilerim ve de Kirazelerimiz Elif Abla, İlknur örtmenim ve minik Deniz'imize,
- başlı başına Esra: her şey için (saymakla bitmez!),
- members of the most joyful research group: İlkin, Sinan, Semih, Selçuk, Atilla, Burcu, Ali, Alman Ahmet, CevriyeBarış, Mmn, Bataş, Köle Zeliha, Murat,
- my co-advisor Rudiger A-Eichel and the dearest friends/colleagues Emre, Ebru and Peter from Technical University of Darmstadt / Freiburg University – Germany,
- Görkem, Serpil Hanım, Efsun Hanım, Nihan Hanım, Bilgen Bey,Zeynep and Ziynet Hanım from the dean of students' office,
- Muharrem Abi for "tatlı kavun" muhabbetleri, technical and motivational support,
- colleagues from the neighboring laboratories that we share common destiny, group spirit, and coffee room,
- all academicians, administrative personnel, instructors, assistants and students mainly, in the science and engineering faculties and then in the whole Koç University,
- TÜBİTAK for their financial support in sake of science,
- Koç family, group and the university to realize this opportunities,
- "itsmylife" İsmail, Cem, Ertuğrul, Moritz, Oğuz, Aytaç, Yük.Mak.Müh. grubu, halkoyunları ekibimiz KUFOLK üyeleri, Ufuk, Şimşir, Osman, Alper, Arican, Ceren, Menekşe, Akif Abi, Seray, Çağlar, Sinem, Sema, uluğ, Rauf, Hüseyin *einşte*in, Zeynep, Özge, Markus for making this life more fun, easier and more valuable,
- Sony PS2 R&D team, IBM, Europcar, Mer Balık, Efes, Duty Free, IETT, nachrichtentreff, Nevizade and Tophane community, yemeksepeti.com, ryan air, milli piyango, cici, divan kafe, biri,
- and everyone I can not list here now for contributing in this study.

TABLE OF CONTENTS

List of Tables

List of Figures

Nomencleature

χ	:	Magnetic susceptibility
$\perp$	:	Perpendicular
θ	:	Incident angle
α,β,γ	:	Angles of unit cell
//	:	Parallel
ΔE	:	Energy difference between two quantized states
Å	:	Angstrom
a,b,c	:	Dimension of unit cell
B_o		External magnetic field
C	:	Base centered cell
CPP	:	Combined Polymerization and Pyrolysis
D	:	Mean grain size
DSC	:	Differential Scanning Calorimetry
DTA	:	Differential Thermal Analysis
E	:	Electron
EPR	:	Electron Paramagnetic Resonance
ESR	:	Electron Spin Resonance
F	:	Face centered cell
FWHM	:	Full Width Half Maximum
g_e	:	Landé – g-factor
h	:	Hole
I	:	Body centered cell
ICSD	:	Inorganic Crystal Structure Database
k	:	Sherrer Constant
KNN	:	Sodium Potassium Niobate
L	:	Ligand
MA	:	Methacrylic acid
MSDS	:	Material Safety Data Sheet

Nd:YAG	:	Neodymium doped yttrium aluminum garnet
NMR	:	Nuclear Magnetic Resonance
P	:	Primitive cell
PT	:	Lead titanate
PVDF	:	Polyvinylidene foluride
PVT	:	Pressure, volume, temperature
PZT	:	Lead zirconate titanate
R_x	:	Ionic radius of X
Tc	:	Curie temperature
TGA	:	Thermal gravimetry
UV	:	Ultra violet
V	:	Vacancy
XRD	:	X-Ray Diffraction
λ	:	Wavelength of the incident beam
μ	:	Magnetic permeability
μ_B	:	Bohr magneton

Chapter 1

Introduction and Theoretical Concepts

1.1 Introduction

Continuous development of technology emerges necessity of advanced materials having extensive and advantageous properties. Oxide materials and advanced ceramics are among the most promising developing materials due to their heat resistance, corrosion resistance, increased strength, hardness and electrochemical properties. The research and development of metal oxides revolutionize the field of material science and technology. Dramatic changes are taking place in applications of these materials which generate improved performance of existing products and enable birth of new technologies [1].

In parallel, nanotechnology studies are on demand since the last decade. Most of the existing materials are developed in nanoscale and their mechanical, optical, electrical and magnetic properties are enhanced. By definition, any material having at least one dimension in the 1-100 nm scale and materials having building blocks in nanosized clusters are called nanomaterial. In theory, as the grain size decreases, there is a significant increase in the volume fraction of grain boundaries or interfaces. This characteristic strongly influences the chemical and physical properties of the material. For example, nanostructured ceramics are tougher and stronger than the coarser grained ceramics. Nanophase metals exhibit significant increases in yield strength and elastic modulus. Using a variety of synthesis methods, it is possible to produce nanostructured materials in the following forms: dots, fibers, thin films, coatings, powders and as bulk materials [2].

1.1.1 Overview on Piezoelectric Crystals

The word of "piezo" is derived from Greek *piezein* which means "to press" or "to squeeze". Piezoelectricity is the ability of some materials notably some crystals, ferroelectric materials and certain perovskite ceramics to generate an electric potential in response to an applied mechanical stress (direct piezoelectric effect). It is a reversible process means a piezoelectric material will undergo a shape change in response to an applied voltage (converse piezoelectric effect). Specifically, the volume change corresponds to maximum 0.1% of the original dimension for lead zirconate titanate (PZT) crystals [3].

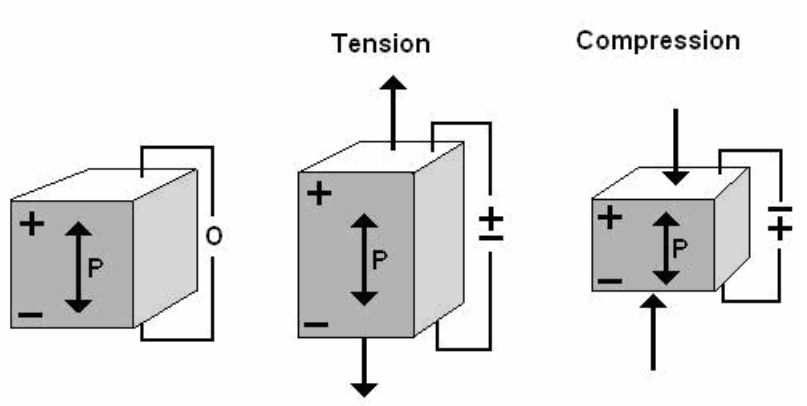

Figure 1.1 Direct piezoelectric effect

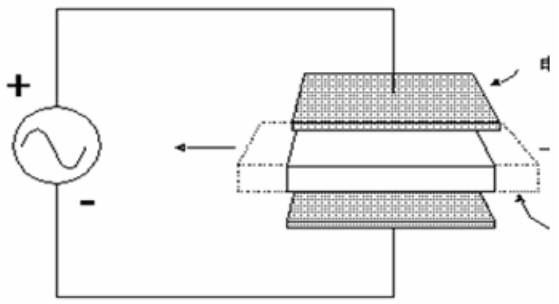

Figure 1.2 Electron flow to piezoelectric stress

In figure 1.1, the stress is applied on crystal and due to the shape deformation direct piezoelectric effect occurs. When a piezo-crystal is squeezed, cationic and anionic centers shifts and a dipole is generated which results current flow as shown in figure 1.2 [4].

Table 1.1 List of well know piezoelectric materials

Name	Formula	Root	Morphology	Structure*
Quartz	SiO_2	Natural	Crystal	Hexagonal
Berlinite	$AlPO_4$	Natural	Crystal	Rhombic
Lithium tantalite	$LiTaO_3$	Synthetic	Crystal	Trigonal
Gallium orthophospate	$GaPO_4$	Synthetic	Crystal	Trigonal
Lead titanate	$PbTiO_3$	Synthetic	Crystal	Tetragonal
Barium titanate	$BaTiO_3$	Synthetic	Crystal	Tetragonal
Bismuth ferrite	$BiFeO_3$	Synthetic	Crystal	Tetragonal
Lead zirconate titanate	PZT**	Synthetic	Crystal	Cubic
Zinc oxide	ZnO	Synthetic	Crystal	Cubic
Aliminum nitride	AlN	Synthetic	Crystal	Hexagonal
Polyvinylidene fluoride	PVDF**	Synthetic	Semi-Crystalline	Thermoplastic
Sodium potassium niobate	KNN**	Synthetic	Crystal	Orthorhombic

* Crystal structures at room temperature

** Well known abbreviations

1.1.2 Focus on Lead Titanate – $PbTiO_3$ (PT)

The simple ABO_3 perovskite compounds such as $PbTiO_3$, $BaTiO_3$, $SrTiO_3$, and $PbZrO_3$ and their solid solutions are archetypal ceramics with a long history of technological application in the electronics industry. Increasing the demands of electronic ceramics has led to greater sophistication in the process of these materials including the powder synthesis stage. Especially lead titanate has been a very attractive material for many years from both scientific and practical aspects because of its highest Curie temperature (T_c = 490°C) and the largest anisotropy (c/a = 1.064 in the tetragonal phase) in the simple perovskite family [5]. It is also initiator of several further research such as shifting one of the titanium cations with zirconium and have well known lead zirconate titanate – PZT ($PbZr_xTi_{(1-x)}O_3$). Moreover, PT compositions have high mode-cancellation (reduced side-load sensitivity) compared to other solid solution piezoelectric materials such as zirconium titanates. The good voltage output constant and excellent mode cancellation of lead titanates are valuable for non-destructive testing, accelerometers and hydrophones [6].

Lead titanate contains 1 lead atom on the 8 corners (1/8 Pb each), 1 titanium atom at the center and 3 oxygen atoms on the 6 faces (1/2 O each) of the unit cell of its ABO_3 type perovskite structure. According to Material Safety Data Sheet (MSDS), it is harmful, hazardous by inhalation, ingestion and skin absorption may cause skin and eye irritation. Thus, the PT should be treated with care and worked under proper apparatus (gloves, googles, clothing, respirator). It is noncombustible, odorless, yellow powder [7].

1.1.3 History and Applications

Although the piezoelectricity concept is discovered during mid-18^{th} century by Carolus Linnaeus and Franz Aepinus, first demonstrations are done by Pierre Curie and Jacques Curie brothers in 1880. However, first practical application of piezoelectric devices was sonar and used in the World War 1. In 1917, French Paul Langewin and his coworkers developed an ultrasonic submarine detector. Simply, a quartz crystal is placed between two large steel panels one of which is fixed and the other one is free to move. When a sound is bounced off an object, vibrations of the echo were detected by the hydrophone with the help of quartz transducer chip and distance to that object could be calculated. This led numerous other applications throughout the history [8].

Main topics of these applications can be listed as sensors, actuators, piezoelectric motors, vibration reducers, high voltage and power sources, frequency standard and powering portable devices recently. For instance, our parking assistance works similar to the first WW1 – sonar application. Due to electric generation in response to stress, one can ignite the fire via a piezoelectric lighter easily. Sound generation is also the most common sensor application of piezocrystals which is used in speakers and other sound devices. Quartz is used as frequency standard due to its direct and converse piezoelectric oscillation. Thus, quartz watches are the most widely used example for converse piezoelectric effect. In most of the advanced tools, extremely accurate and small piezoelectric motors are used. Most recently, multitouch screens relies on piezoelectricity concept. Since ferroelectricity and piezoelectricity are close phenomena, they both serve as applicable electro chemicals. One significant use of ferroelectricity is achieved by Fujitsu in the F-RAM technology. Ferroelectric RAM (FeRAM or FRAM) is non-volatile, and it requires lower power to operate which enables much faster write-

erase cycle speed. Non-volatility for a storage system means information can be stored even without power supply. Hard disks, floppy disks, USB flash disks are well known examples for non-volatile memory group.[8]

1.1.4 Purpose of the Research

In general, metal oxide compounds are highly interested due to their ferroelectric and piezoelectric properties. Doping into crystal structure shifts the lattice order which results an improvement on magnetic properties and dielectric constant. As well as, grain size crucially impacts the characteristics of the material which can be optimized via syntheses parameters.

Specifically, size variation in Fe^{3+}-doped $PbTiO_3$ nanopowders is aimed to be done by various thermal and mechanical treatments in this study. It is announced that Cr^{3+}-doped $PbTiO_3$ nanopowders polymerize at 260°C and pyrolysis occur at above 350°C [9]. For our case, slight increments in between 300-400°C and further observations till 900°C will be examined in different trials. Fe^{3+} will be used as dopant and nanopowder grain size is expected to vary in the range of ~10 – 100 nm. Experimentally, the precursor is prepared via sol-gel method and then it is dried and get prepared for calcination. Calcination is done via combined polymerization and pyrolysis route. Different calcination time and temperatures are experimented to obtain the smallest grain size with lowest reaction temperature. Furthermore, the product is ball-milled for even smaller grain sizes.

In particular, $PbTiO_3$ has tetragonal crystal structure with a 1.06 c/a ratio and shows paramagnetic property at room temperature. When the compound is heated above its T_c which is 490°C, then the crystal structure transforms from tetragonal to cubic phase by enlarging the unit cell dimensions. The anionic and cationic centers match and crystal becomes diamagnetic. Our goal is try to reduce the c/a ratio and generate cubic PT crystals at room temperature.

The sample characterization is based on X – Ray powder diffraction, Raman scattering, X – Band Electron Paramagnetic Resonance and Thermal Gravimetry and Differential Thermal Analysis techniques.

1.2 Theoretical Concepts

For a better understanding of this study, some of the main concepts are better to be rehearsed first. Perovskite structures, ferroelectricity, piezoelectricity, defect chemistry, Kröger – Vink Notation, acceptor and donor type of doping and defect dipoles are among them.

1.2.1 Crystal Structures

A lattice is a periodic arrays of "dots" (atoms) or lattice points which is a mathematical abstraction used to describe the translational symmetry of an extended periodic structure. The simplest representative portion of a lattice which can be repeated and cover the entire 1-D, 2-D or 3-D space is called *unit cell*.

In 3-dimensional space, depending of the constants (a,b,c) and angles (α,β,γ) 7 different crystal systems can be defined: cubic, tetragonal, orthorhombic, hexagonal, trigonal, monoclinic and triclinic. In addition to these 7 primitive cells (P), body centered cell (I) contains two, face centered cell (F) contains four and base centered cell (C) contains two lattices, named as the Bravias Lattices. (Table 1.2)

Table 1.2 Crystal Systems and Bravias Lattices

Crsytal System	**Bravias Lattices**
cubic	P, I, F
tetragonal	P, I
orthorhombic	P, I, F, C
hexagonal	P
trigonal	P
monoclinic	P, C
triclinic	P

In crystal chemistry, notations of "a", "b" and "c" are used for the dimensions of the unit cell and they are called constants whereas "α", "β" and "γ" are the angles in lattice parameters. For a cubic cell, dimensions are a = b = c and a tetragonal cell it is a =

b ≠ c. So, the c/a ratio corresponds for the height / base sides of a tetragonal prism. (Table 1.3)

Table 1.3 Types of Unit Cells

CUBIC	TETRAGONAL	ORTHORHOMBIC	HEXAGONAL
a=b=c	**a=b≠c**	**a≠b≠c**	**a=b≠c**
α=β=γ=90°	α=β=γ=90°	α=β=γ=90°	α=β=90°,γ=120°

TRIGONAL	MONOCLINIC	TRICLINIC
a=b=c	**a≠b≠c**	**a≠b≠c**
α=β=γ≠90°	α=γ=90°,β≠120°	α≠β≠γ≠90°

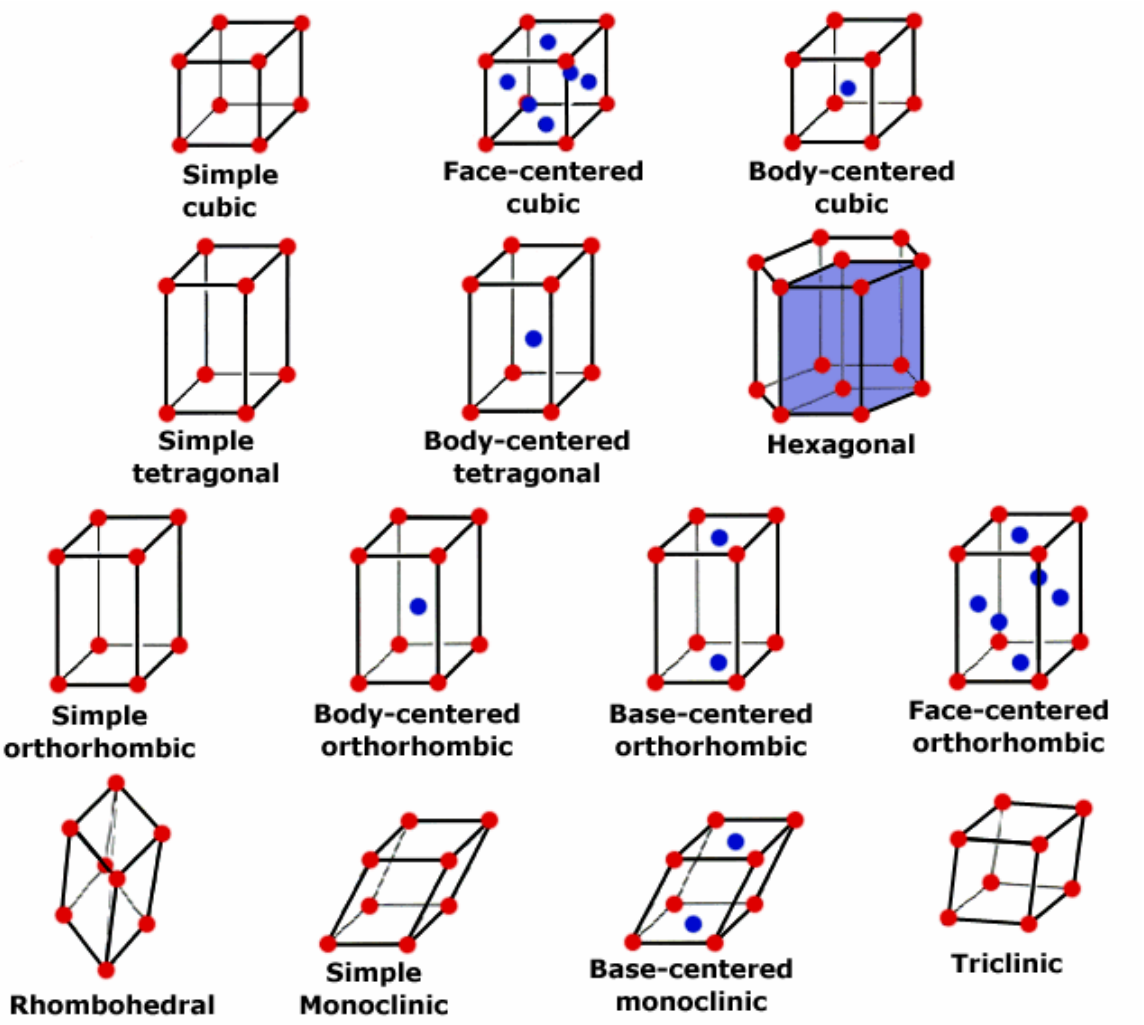

Figure 1.3 14 Bavarias Lattices

1.2.2 Perovskite Structure

Perovskites take their name from the compound of $CaTiO_3$ which is known as *perovskite structure* [10]. The perovskite-like structure is a ternary compound of formula ABX_3 that A and B cations differ in size (A atoms are larger than B) and X is the anion that bonds both. The most common perovskite compounds contain oxygen on the X-site, however, there are a few perovskite compounds formed without oxygen ($NaMgF_3$ for instance). It is considered an FCC- derivative structure in which the larger A cation and oxygen together form an FCC lattice while the smaller B cation occupies the octahedral interstitial sites in the FCC array. The ideal cubic-symmetry structure has the B cation in 6-fold coordination, surrounded by an octahedron of anions, and the A cation in 12-fold cuboctahedral coordination [11]. Specifically, $PbTiO_3$ has perovskite-like structure. 8 Pb^{2+} atoms lay on all corners (8*(1/8)=1 atom/cell), octahedral 6 oxygens on the faces (6*(1/2)=3 atom/cell) and one tetrahedral Ti^{4+} cation (1 atom/cell) is positioned in the center as can be seen in figure 1.4 [12].

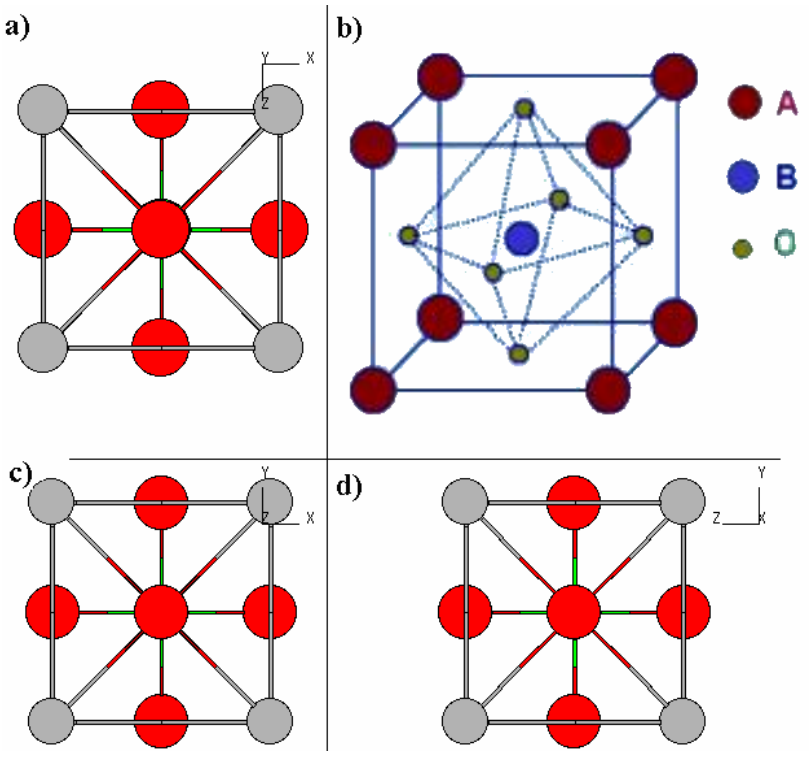

Figure 1.4 Perovskite Structure a), b) and d) are side views from y,z,x respectively. b) is angled view.

When perovskite structure is distorted, its symmetry is reduced which has significant impact on magnetic and electrical properties. Vacancies, dopants and temperature are main factors causing cell distortion. Degree of distortion is tried to be estimated and formulized by Goldschmidt in 1926. Structure stability is handled mostly in $0,78 < t < 1,05$ values for perovskites. Symmetry is reduced with t value [13]. "t" value is Goldschmidt Tolerance Factor which is shown in equation 1.1 where R_A is the ionic radius of A, R_B is the ionic radius of B, and R_O is the ionic radius of oxygen at ABO_3 perovskite structure.

$$t = (R_A + R_O) / \sqrt{2}\ (R_B + R_O)$$

Equation 1.1 Goldschmidt Tolerance Factor

$$t = (R_{Pb} + R_O) / \sqrt{2}\ (R_{Ti} + R_O)$$

Equation 1.2 Goldschmidt Tolerance Factor for $PbTiO_3$

Equation 1.2 can be derived for our case. According to calculations, when t = 1 ideal cubic symmetry is expected.

As can be seen in figure 1.5, the lattice is not exactly cubic but slightly distorted. Central cation, Ti^{4+} does not positioned at the exact center but slightly off to one side in z direction along c dimension. Thus, perovskite structure carries a dipole moment which leads to ferroelectric property and this fact crucially changes the complete nature of the compound.

1.2.3 Ferroelectricity

Ferroelectricity is a spontaneous electric polarization of a material that can be reversed by applying an external electric field. Certain nonconducting crystals, or dielectrics, that exhibit spontaneous electric polarization (separation of the centre of positive and negative electric charge, making one side of the crystal positive and the opposite side negative) that can be reversed in the direction of applied external electric field. Ferroelectricity is named by analogy with ferromagnetism, which occurs in such materials as iron. Iron atoms, being tiny magnets, spontaneously align themselves in clusters called ferromagnetic domains, which in turn can be oriented predominantly in a given direction of externally applied magnetic field [14,15]. When cationic and anionic

centers do not coincide, dipole occurs in unit cell which leads ferroelectric property as shown in figure 1.5 [16].

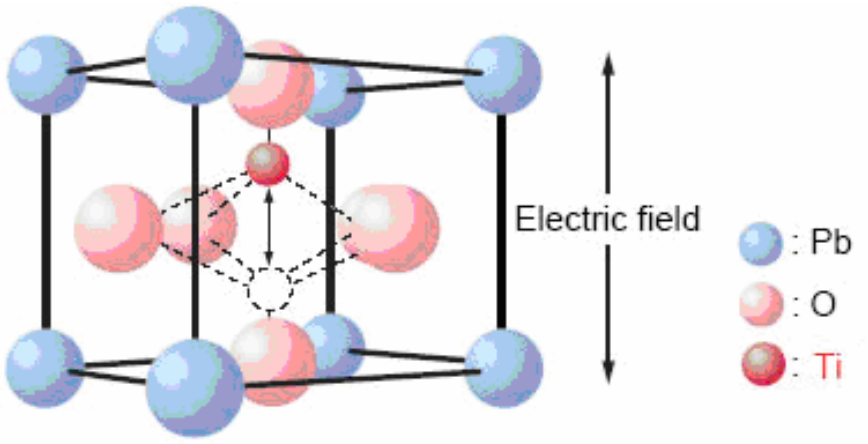

Figure 1.5 Ferroelectricity in $PbTiO_3$ unit cell.

It is also known that all ferroelectrics are required by symmetry considerations to be also piezoelectric and pyroelectric.[17]

1.2.4 Defect Chemistry

Crystal defects and solid imperfections are great topics of interest in physics and chemistry. Since Fe^{3+} dopant is used in our system to enhance electrical property of $PbTiO_3$, defect chemistry should be analyzed even roughly. Defects in crystalline materials are categorized by dimensionality as point, line planar and volume defects, by type of vacancies as self interstitials, substitutional impurities, interstitial impurities, Schottky, anion Frenkel and cation Frenkel, respectively.

When an atom is substituted by another atom, size difference causes vacancies and several electric changes occur under specific conditions like our case where the dopant Fe^{3+} replaces Ti^{4+} position and then oxygen vacancy occurs, generating point in crystal systems (Figure 1.6.a). For a clear definition of those circumstances, a specific notation is proposed by F. A. Kröger and H. J. Vink, called *Kröger – Vink Notation*.

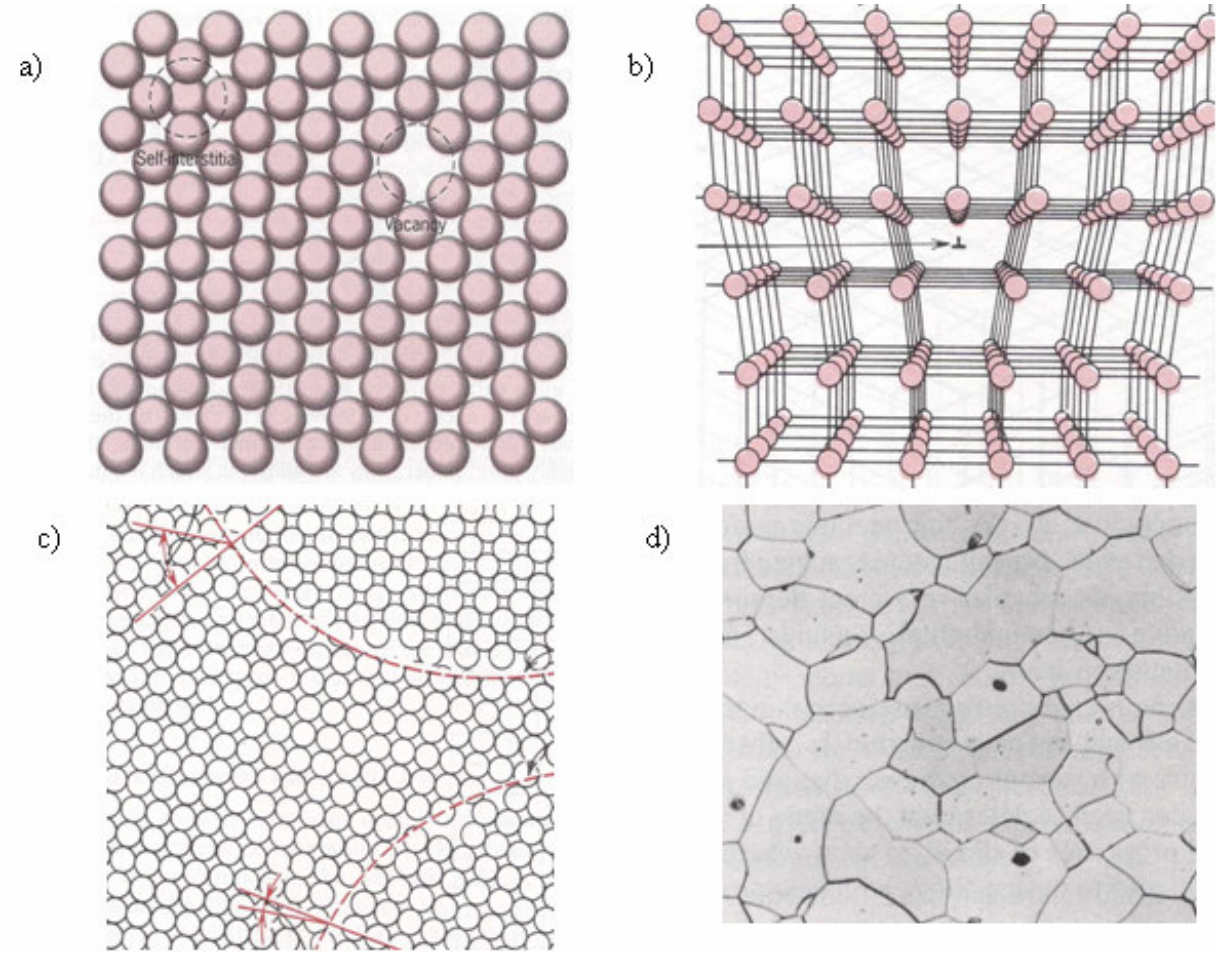

Figure 1.6 Crystal Defects a) point, b) line, c) plane, d) volume

1.2.4.1 Kröger – Vink Notation

M_S^C means that M sits on the S site on lattice with C charge. M can be the symbol of any element, vacancy (V), electrons (e) or a hole (h). "i" indicates lattice interstice. S indicates the lattice site that species occupies and can be notated as the symbol of element or just a lattice interstice with the symbol "i". C is the sign for the overall electronic charge difference. Relative charge comparison of the species and the site that it occupies defines the C value. It has specific notations like X for neutral case, $\bullet$ for single positive charge and $\bullet\bullet$ for double positive charge. On the contrary, when ‘ is used instead of $\bullet$, then it implies single negative charge (electron), where “ is for double negative charge (electrons).

For instance, when Na^+ ion is substituted by Ca^{2+} ion, then calcium cation sits on sodium place which has one more positive charge and it is notated as $Ca_{Na}^{\bullet}$. Similarly, for instance when a copper atom is replaced by a nickel than it is notated as Ni_{Cu}^{X}. Here, since the charges of Ni and Cu are equal, the overall net charge would be zero, represented with an X. In the last instance, a chloride ion is removed and its site is not filled, means vacancy occurs in chloride position. In this case, the net charge change would be +1 notated with a $\bullet$. Overall Kröger – Vink notation would be as $V_{Cl}^{\bullet}$ for the third example.

1.2.4.2 Acceptor and Donor Type of Doping

Doping is defined as the addition of impurities to a crystal or semiconductor lattice to control and alter the electrical, optical and mechanical properties mostly in semiconductors. In general, any trace amount of additive to a media for a purpose such as changing the material property (conductivity, electrical resistivity, refraction index) or enabling the tracking of a change can be defined as doping.

In physics, doping is divided into two categories according to the electrical charge of dopant: donor type of doping and acceptor type of doping.

In case that the doped impurity has more protons thus more electrons per atom than the stationary element, then there will be additional electrons which are loosely bonded and more free to move in comparison to closed shell bonded electrons. Therefore, due to additional electron, dopant carries negative charge and it is called *donor type of doping*. Vice versa, when the impurity has fewer electrons, then there will be reduced electron density in the new scenario, and media will be positively charged which is named as *acceptor type of doping*.

Not only changing material property, but also tracking functionality of a dopant is significant advantage of doping. For instance, $PbTiO_3$ is EPR inactive sample because of not having a paramagnetic species in structure. However, when an Fe^{3+} is added to $PbTiO_3$ it makes the compound EPR active because iron has unpaired electrons in d^5 orbital that enables the tracking of the doped unit cell property.

Chapter 2

Experimental Part and Characterization Techniques

2.1 Experimental Synthesis Techniques

Various powder synthesis methods progressed with the extraordinarily developing technologies throughout the history. According to different necessities and aspects, some of the methods might be more practical than the others. However, all methods have different pros and cons some of which can be followed in table 2.1 [17].

In this section, some of the different experimental techniques will be analyzed in detail such as the method that I used which can be categorized under polymerizable complexes, and other alternative synthesis methods such as solid state reactions, hydrothermal technique and sol-gel reaction.

Table 2.1 Comparison of various powder synthesis methods

Parameter	Solid State Reactions	Sol-Gel	Polymerizable Complex	Hydrothermal
Cost	Low to moderate	High	High	Moderate
State of Development	Commercial	R&D	R&D	R&D/ demonstration
Compositional Control	Poor	Excellent	Excellent	Good/excellent
Morphology Control	Poor	Moderate	Moderate	Good
Powder Reactivity	Poor	Good	Good	Good
Purity (%)	<99.5	>99.5	>99.9	>99.5
Calcination Step	Yes (multiple)	Yes	Yes	No
Milling Step	Yes (multiple)	Yes	Yes	No

There are also co-precipitation and laser excited sintering methods which are rarely used but not mentioned in detail here. Although, some of the methods listed here sound similar and used alike chemistry, advanced materials' synthesis requires different treatment during preparation which crucially affects the overall material property, thus subdivisions of synthesis techniques will be presented in the following sections.

2.1.1 Polymerizable Complexes Reaction

This is the route used during this study. Although, the closest category is polymerizable complexes reaction, it is the combination of several principles and different methods. In this method, complex compound is prepared as starting precursor which has polymerizable multiple bonds in its structure or forms metal-oxo, metal-hydroxo chains. After excitation via thermal or laser source, polymerization starts as the transition from amorphous precursor morphology to ordered crystal lattices. Since most of the organics are volatile at relatively lower temperatures, product purity is increased after the vaporization of organic part of the precursor. More than 99.9% purity can be obtained via polymerizable complexes route. Instead of industry, mostly research and development based institutes prefers this method because of its high cost, relatively lower production quantity, and multi-stepped synthesis [18].

Combined polymerization and pyrolysis route (CPP Route) also depends on the similar origin. However, CPP has a special advantageous feature which is the ability to introduce paramagnetic probe ions. So far, several studies succeeded to produce 12 nm sized nanoparticles of $PbTiO_3$ synthesized via this method [19]. Among disadvantages of this process, high cost, multi-stepped reaction mechanism and non-environmental properties of organics can be counted.

2.1.2 Solid State Reactions

Solid state reaction technique is the most conventional and widely used technique in metal oxides' synthesis. In this method, powder reactants (usually simple binary oxides or pure elements) are literally mixed in a cruicible or an ampoule and then heated up to elevated temperatures. Reactants either remain in solid phase and react with each other or undergo phase transformation from solid to liquid state, then reaction occurs.

Regarding the purpose, inert atmosphere can be selected where the solid mixture is placed in enclosed steel or niobium ampoules which are sealed and vacuumed to avoid high temperature explosions.

For instance, for lead titanate synthesis, stoichiometric combinations of elemental lead and titanium or lead oxide and titanium oxides can be taken and heated up to 1200°C degrees in an open atmosphere setup. Due to higher thermal energy, bulky grain growth occurs and particle size would be in the order of micrometer.

This technique involves some problems such as vaporization of certain starting oxides at elevated temperatures (e.g. PbO, >880°C). PbO vaporization does not only changes stoichiometry but also poisons the environment because of its hazardous and toxic properties. Also, solid reactions require high temperatures which are costly. In addition, while increasing the annealing temperature, the morphology, compositional control and powder reactivity become poorer [20].

2.1.3 Hydrothermal Processing Technique

Hydrothermal technique can be defined as any homogeneous or heterogeneous chemical reaction in the presence of a solvent (whether aqueous or non-aqueous) above the room temperature and at an elevated pressure which is greater than 1 atm in a closed system [21]. The known largest single crystal, beryl crystal, formed by nature weighs >1000kg, and largest quantity of man made single crystal, quartz crystal, in one experimental run weighs several 1000s kg that are both of hydrothermal origin [22].

Hydrothermal process depends on the PVT (pressure, volume, temperature) ratio. According to physic basics, collision in a medium is directly proportional to pressure and temperature while inversely proportional to volume of the container, so at high pressure and high temperature higher collisions are generated. In this technique, a steel vessel, called *autoclave* (Figure 2.1), that is highly pressure resistant closed system is heated and used as reaction setup (Figure 2.2). As reported in the literature [24], in order to synthesize $PbTiO_3$ via hydrothermal process, the reaction took place in a 300 ml reaction vessel under 5,07 MPa (50,04 atm) pressure at 200°C for 2 hours. The starting materials lead nitrate and titanium tetrachloride are dissolved in distilled water and diluted.

Mixture of several organics used as solvent and catalysts [23]. In this method, the particle size is reported to be in the range of 100 – 400 nm [24].

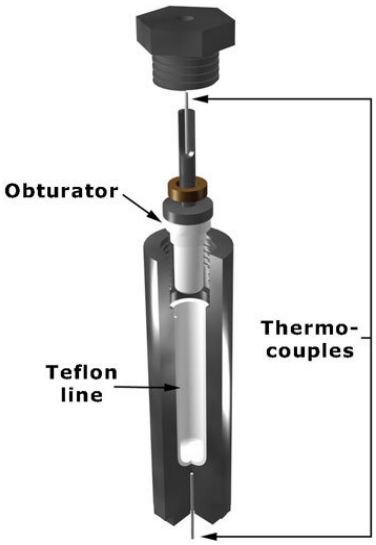

Figure 2.1 Hydrothermal reaction vessel (autoclave) – left

Figure 2.2 Hydrothermal Synthesis Setup– right

Obviously, hydrothermal technique provides excellent possibility for processing of advanced materials. For instance, reaction temperature is reduced to a few hundred celcius degrees by increasing pressure which affects lattice properties and particle size. On the other hand, the technique has some handicaps such as requiring a specific setup which is moderately costly, as well as resulting a fair composition control and product purity in comparison to other methods.

2.1.4 Sol-gel Method

Abbreviation of *sol* and *gel* corresponds to solution and gelation respectively. Sol-gel is wet-chemical technique for the fabrication of materials. Since the starting materials of this type of reactions are chemical solutions or colloidal particles, *sol* is named for reactant and since an integrated network formation is aimed, *gel* is defined as end product meaning gelation. For instance, typical precursor of metal alkoxide and metal chlorides undergoes hydrolysis and polycondensation reactions to form metal-oxo

(M-O-M) or metal-hydroxo (M-OH-M) bridges in solution. Typical sol-gel process ends up with thermal treatment to favor further networking and enhance mechanical properties [25]. A general diagram about sol-gel method can be seen in figure 2.3.

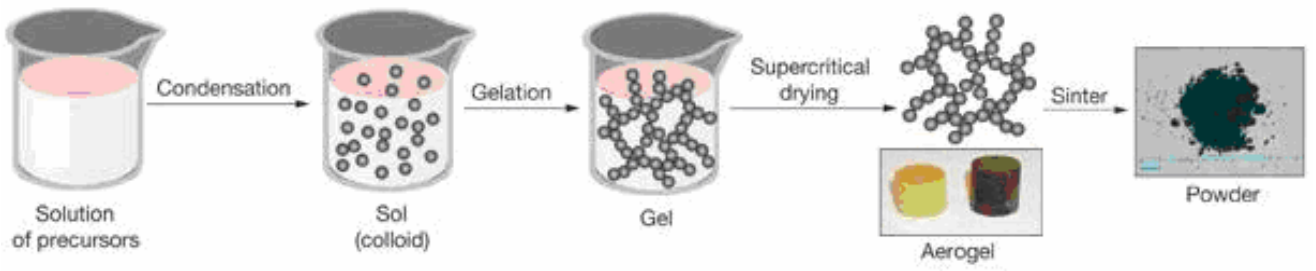

Figure 2.3 Sol-Gel Chemistry

In order to produce $PbTiO_3$ specifically, titanium isopropoxide ($Ti[(CH_3)_2CHO]_4$) and lead acetate $Pb(CH_3COO)_2.3H_2O$ solution mixture can be taken which is catalyzed with hydrochloric acid for gelation. Then gel is dried around 125°C and grinded to powder. Further polycondensation can be done both via sintering or laser-annealing [26]. Mostly, particle sizes are recorded around 10 nm while dry gel form, however, it increases up to 100 nm after thermal treatment.

Due to organic reactants and condensation principle, the method is versatile. Also, pure and homogeneous mixtures of nanoparticles can be obtained because of the solution based environment. Powders become more reactive than solid mixture resembles thus lower sintering temperatures can be obtained. Yield purity and morphology control is still moderate in table 2.1. Also, usage of organic solvent may cause solubility limitations and toxicity handicaps.

2.2 Characterization Techniques

Characterization is the use of advanced equipments and techniques to investigate the internal structure and the properties of the materials. Characterization techniques function for magnification and internal visualization of structures. They are used to make elemental, quantitative and qualitative analysis of chemicals. As well as, distribution and interaction of the inner particles can be examined. There are various characterization

techniques are in use for distinctive purposes. In the scope of my thesis, I will present only these methods which I employed during my study, these are X – Ray Powder Diffraction (XRD), Raman Spectroscopy, Electron Paramagnetic Resonance (EPR), Thermal Gravimetry and Differential Thermal Analysis (TG / DTA).

2.2.1 X – Ray Diffraction

X – Ray Diffraction is one of the most fundamental analysis methods to determine the crystal structure and atomic arrangement of crystalline compounds. It involves mainly X – Ray Powder Diffraction which is applied to crystalline or semi-crystalline powder samples; and X – Ray Single Crystal Analysis which is applied to single crystals. Other rarely used forms of the technique are X – Ray Fiber diffraction and Small-angle X – Ray Scattering (SAXS). Specifically, X – Ray Powder Diffraction method is used during this study.

By using powder diffraction method, one can:

- Verify the compound
- Identify the specimen content
- Determine space group and crystal structure
- Calculate the purity, electron density, particle size and lattice parameters
- Designate the mean positions of atoms

In order to generate X – Ray waves, an X – Ray tube is used in which rapidly moving electrons hits solid target and the energy conversion occurs from kinetic energy to radiation. The efficiency of this process is around 1% and most of the energy is converted into heat in X – Ray tube which is supposed to be cooled well during wave generation to avoid anode meltdown [27]. In this study, X – Ray powder diffraction analysis was performed by using Huber G670 that is equipped with a germanium monochromator and $CuK_{\alpha 1}$ radiation which has the wavelength of *1.5405929 Å* [28]. Electromagnetic spectrum involves several types of waves changing with respect to their wavelengths. X – Ray radiation is preferred in such studies because the wavelength lies within the range of 1.10^{-9}m – 1.10^{-11}m (Figure 2.4) which corresponds to the scale of the atom size, radii of ions and the distance between the lattices in the crystals [29].

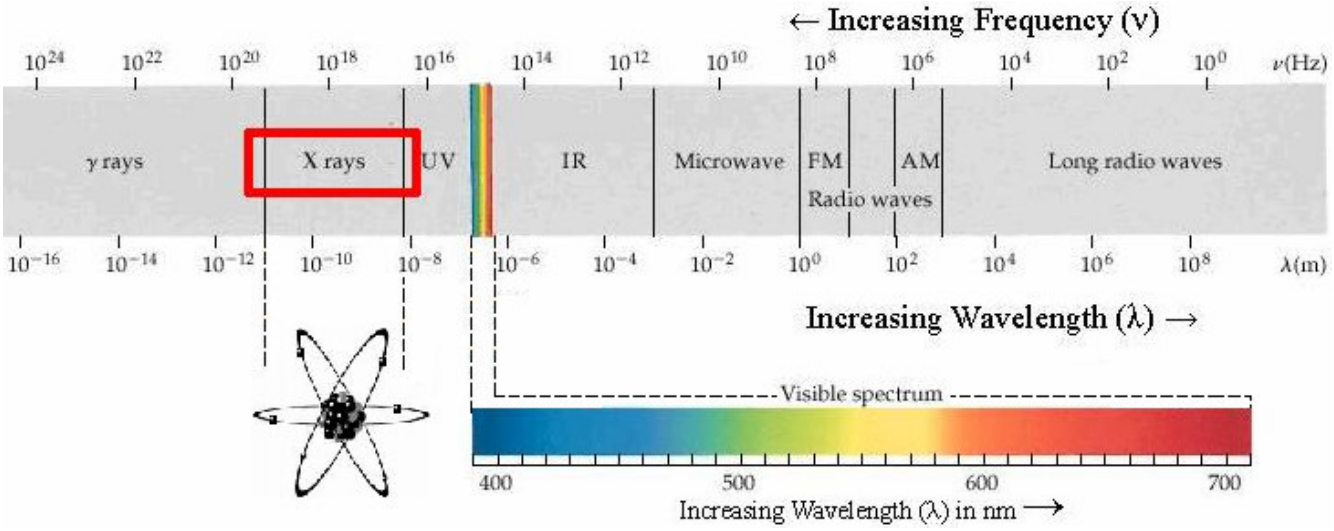

Figure 2.4 Electromagnetic Spectrum

After the radiation generation in the X – Ray tube, X – Ray radiation is transmitted upon the crystal sample and there it partially scatters of electromagnetic waves on electron sheath of atoms. In other words, when radiated wave hits the atoms sitting on the crystal layers it is reflected back at a certain angle [30]. Since the scattering occurs in several layers, the distance in between layers can be calculated via Bragg's Law (Equation 2.1) [31] and this phenomenon can be clearly seen in figure 2.5.

$$2\, d_{hkl}\, \sin\theta_{hkl} = n\, \lambda \qquad \textbf{Equation 2.1}$$

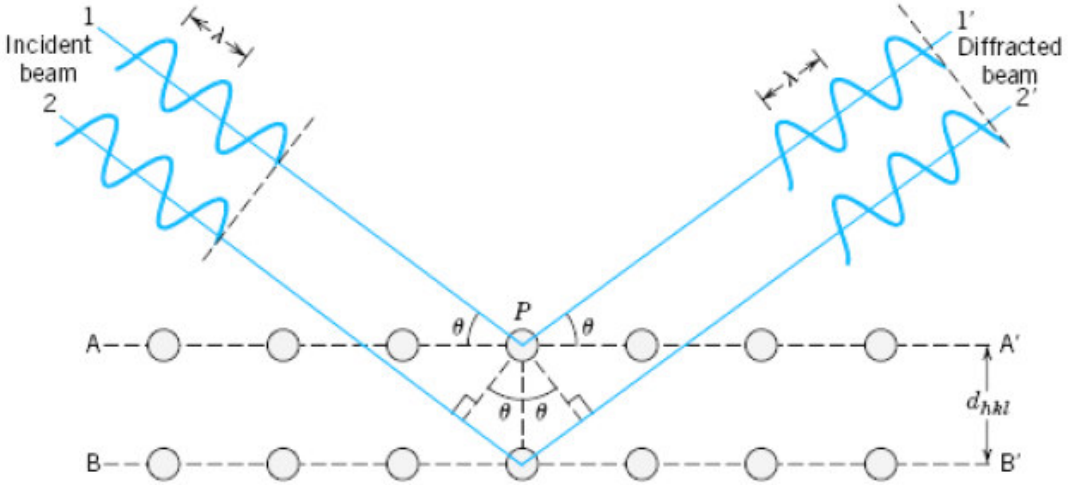

Figure 2.5 The Bragg phenomenon for X – Ray diffraction on crystal lattice

Step size of data collection angle 2θ is 0.005° and it is altered in the range of 3° ≤ 2θ ≤ 100°. When experimental powder pattern is obtained, it is compared with the ones in crystal structures' database such as Inorganic Crystal Structure Database (ICSD) [32] and analyzed with Search / Match function in Stoe WinXPOW software [33].

Moreover, Debye – Scherrer method which is used for characterization of compounds in powder form like metal oxide nanoparticles is applied to measure the crystal size during this study [34].

$$\beta_{hkl} = K \lambda / L_{hkl} \cos \theta \qquad \textbf{Equation 2.2}$$

The crystal lattice is assumed to be "perfect" meaning defects are not taken into consideration during size calculations [35]

.

2.2.2 Raman Spectroscopy

Raman spectroscopy is one of the most fundamental characterization techniques mainly in chemistry and physics disciplines. It analyses vibrational, rotational and other low frequency modes in the crystal systems. It is applied to determine the structure and to analyze multi-component system qualitatively and quantitatively [36]. Raman spectroscopy originates inelastic scattering (so called Raman Scattering) of monochromatic light in the visible, near IR or near UV range and it is based on the energy difference of incident photon and Raman scattered photon that corresponds to the energy of vibration of scattering molecule. This phenomenon is called Raman Effect. Electric dipole is the key concept in Raman Effect because when a photon is incident on a molecule, it interacts with the electric dipole of the molecule. Most of the photons scatters from a molecule elastically (without energy change) called Rayleigh Scattering however, approximately 1 in 10^7 fraction of photons are absorbed or emitted due to structural vibrations which ends up with the energetically shifted photon that gives information about the phonon modes in the system [37]. Molecules either gain energy (Stokes Scattering) or loose energy (Anti-Stokes Scattering) as shown in figure 2.6.

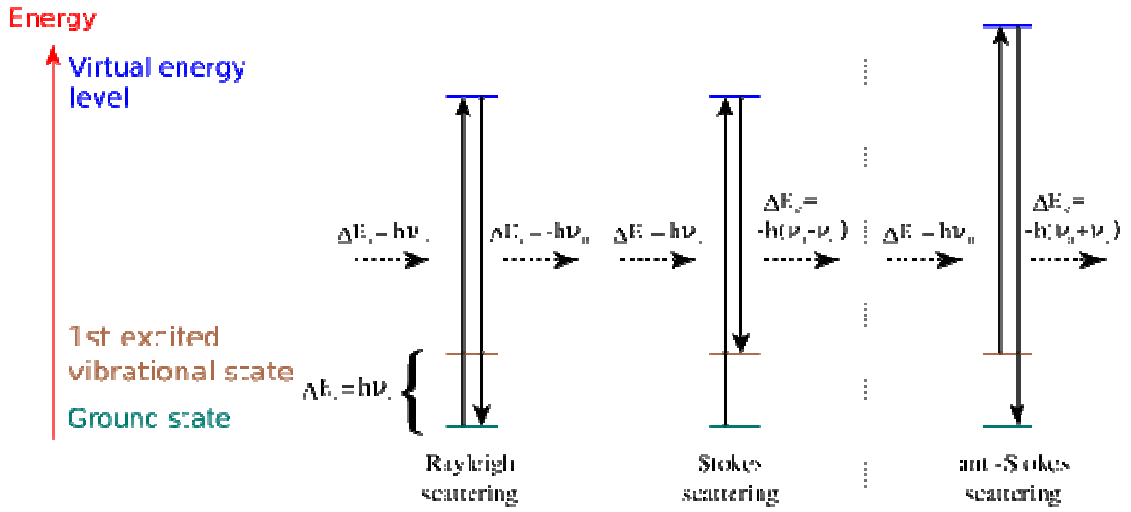

Figure 2.6 Stokes and Anti-Stokes Raman Scattering

During this study, FT-Raman spectra are taken by using Bruker RFS 100/S spectrometer (Nd: YAG-Laser, 1064 nm, 200 mW). Powder samples are filled into the pyrex tubes having 4mm diameter. OPUS^{TM} software is used for data handling.[36] In addition to conventional application of Raman Spectroscopy, ferroelectricity information for $PbTiO_3$ studies are also recorded by analyzing soft mode region.

2.2.3 Electron Paramagnetic Resonance

Generally electron paramagnetic resonance (EPR) spectroscopy provides information concerning electronic and structural properties of free radicals and paramagnetic ions. In particular, important aspects of the defect chemistry and the local defect structure at the site of the functional center can be explained [38]. It is also known as electron spin resonance (ESR). Basic physical concept show high similarity to nuclear magnetic resonance (NMR) however, electron spins are excited in EPR while it is atomic nuclei spins in NMR. Since most of the stable molecules have all paired electrons, application of EPR is limited but due to its high sensitivity and great specificity upon paramagnetic species, EPR technique plays key role in related studies including ours.

In principle, every electron has a magnetic moment and spin quantum number s = 1/2 with two probable magnetic components m_s = -1/2 (parallel to the magnetic field) and m_s = +1/2 (anti-parallel to the magnetic field) in the presence of an external magnetic field with a B_0 strength. Thus, there exists a separation between two energy states (Figure 2.7) which can be formulized as:

$$\Delta E = g_e \mu_B Bo \qquad \textbf{Equation 2.3}$$

where g_e corresponds to so called Landé – g-factor, μ_B is the bohr magneton and B_o is the external magnetic field strength. Formula 2.3 can be derived to 2.5 by using well known energy formula in 2.4.

$$E = h \nu \qquad \textbf{Equation 2.4}$$

$$h \nu = g_e \mu_B B_o \qquad \textbf{Equation 2.5}$$

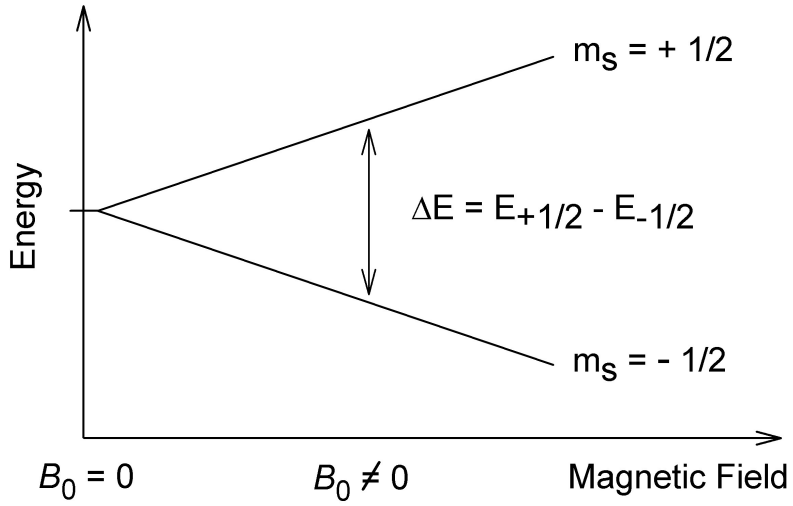

Figure 2.7 Splitting of electron spin states.

Regarding to the application different strength of magnetic fields can be used in order to generate the energy difference between electron spin states and increase resolution to get more detailed spin information. Various EPR bands and the strength of the spectrometer can be seen in table 2.2 [39].

Waveband	**L**	**S**	**C**	**X**	**P**	**K**	**Q**	**U**	**V**	**E**	**W**	**F**	**D**	**—**	**J**	**—**
λ / mm	300	100	75	30	20	12.5	8.5	6	4.6	4	3.2	2.7	2.1	1.6	1.1	0.83
ν / GHz	1	3	4	10	15	24	35	50	65	75	95	111	140	190	285	360
$\boldsymbol{B_0}$ **/ T**	0.03	0.11	0.14	0.33	0.54	0.86	1.25	1.8	2.3	2.7	3.5	3.9	4.9	6.8	10.2	12.8

Table 2.2 EPR Band types and different spectrometer strengths

In our study, EPR characterization played significant role to explain the paramagnetic iron position in perovskite structure. The information about the unit cell it is doped in can be taken via this method. Specifically, X-band (9.5 GHz) continuous-wave EPR measurements were performed by using Bruker ESP 300E spectrometer equipped with a rectangular TE_{112} resonator.

2.2.4 Thermal Gravimetry and Differential Thermal Analysis

Thermal gravimetry (TG) is a well known and widely used method of measuring weight loss of a heated sample as a function of temperature. It gives information about the reaction temperature, yield ratio, phase changes and the weight loss. The measurement media can be adjusted (under air, N_2, etc). Similarly, differential thermal analysis (DTA) is another complementary analytical technique which analysis the required heat change with respect to the temperature. Thus, the information about the exact amount of energy released or absorbed during a chemical process is recorded. An inert reference which is under identical conditions with the sample is used for comparison [40]. During this project, NETZSCH DTA 404 thermal analysis machine and NETZSCH Proteus 4.0 beta software are used. Sample is heated from room temperature to 500°C by applying 5°C increments in every minute.

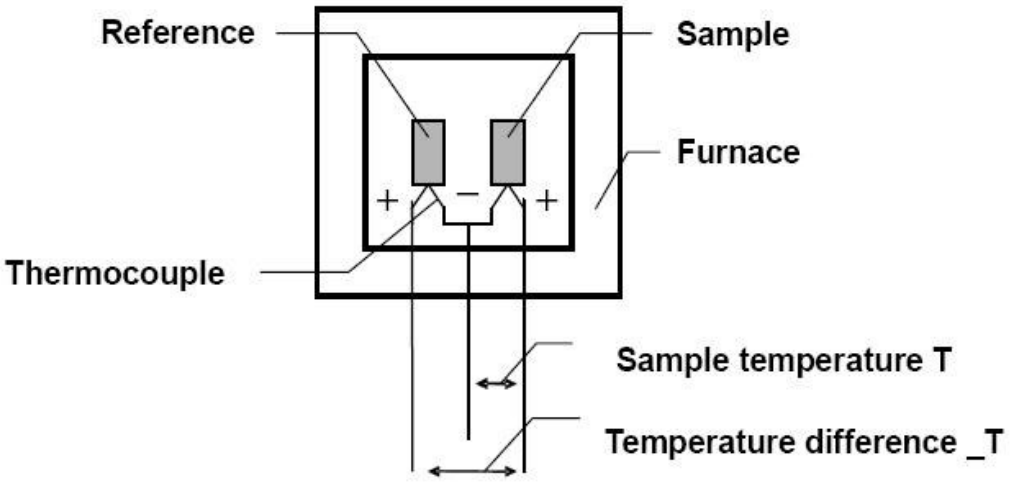

Figure 2.8 Configuration of a DTA device

In figure 2.8, detailed explanation of a regular DTA device can be seen. When the equipment applies energy gradually on both the reference and the sample, the given energy would be used either to increase the temperature or to complete the phase change, reaction, evaporation etc. Thus, temperature change occurs if there is no energy emission or temperature stays still if there is a reaction at the exact energy level.[40]

Chapter 3

Experimental Procedure

3.1 Synthesis of $PbTiO_3$

In this study, primarily size effect of ferroelectric metal oxides upon material properties is examined. To be able to synthesize nano scale perovskitic materials, we applied special method which is one of the most practical (size control by temperature) and efficient methods known as combined polymerization and pyrolysis route (CPP). Also, paramagnetic metal ions (Fe^{3+}, Cr^{3+}, Mn^{2+}, etc.) are easily incorporated to $PbTiO_3$ struce via this method. The Fe^{3+}- modified $PbTiO_3$ nanocrystals were prepared by CPP route of metallo-organic precursors [41], which is generally preferred to synthesize doped perovskitic ultra-fine powders [42, 43].

The main advantages of CPP route are the easy incorporation of transition-metal ions, the requirement of comparatively low crystallization temperatures (below 400°C) and the simplicity of controlling the particle size by adjusting the preparation temperature. This method gives good surface morphology, phase purity and non-agglomerated nanoparticles.[41] The main drawback of this route is, however, that no $PbTiO_3$ nanoparticles with mean grain size below the critical size (~10 nm) can be synthesized. In order to circumvent this shortcoming, short-time soft milling of a parent nanopowder obtained from a tempering route at medium temperature has been subsequently performed, giving particles with mean grain size below 10 nm. With the help of minimal mechanical energy requirement, it is possible to reduce the particle sizes below 10 nm [44].

3.2 Materials and Chemicals Used

Table 3.1 List of reactant chemicals used.

Name	Formula	Supplier	Product Nr.
Lead (II) Oxide	PbO	Sigma-Aldrich	211907
Titanium isopropoxide	$Ti(O\text{-}C_3H_7)_4$	Sigma-Aldrich	377996
Methacrylic acid*	$CH_2=C(CH_3)\text{-}COOH$	Sigma-Aldrich	155721
Iron (III) acetylacetonate	$Fe(CH_3COCH=C(O\bullet)CH_3)_3$	Sigma-Aldrich	517003
Chloroform	$CHCl_3$	Sigma-Aldrich	------

* 250 ppm 4-methoxy phenol is inhibited to avoid polymerization.

3.3 Experimental Part

In detail, the CPP route is based on a route for synthesizing of nanoferrites [45] and involves the following two stages:

i) Preparation of metallorganic precursor

ii) Polymerization and pyrolysis.

3.3.1 Preparation of metallorganic precursor

The chemicals used in these processes are listed in table 3.1. Due to the synthesis conditions (for instance: open system), a certain loss of the lead component had to be taken into account, and for a corresponding compensation, 10% surplus of PbO was added. Iron (III) acetylacetonate was employed as dopant source of Fe^{3+} which is readily soluble in chloroform. Specifically, by mole ratio, 10^{-4} Fe^{3+} / 1 Ti^{4+} (100 ppm) is added as dopant in order to make sample EPR active. Metallo-organic precursor: Lead titanylmethacrylate was obtained as a monomeric metallo-organic precursor from lead oxide, titanium (IV) isopropoxide and methacrylic acid in the reflux system of chloroform ($CHCl_3$) (magnetic stirring, 3h, 61°C) by four stepwise reactions as described in equations part. Since methacrylic acid contains 250 ppm 4-methoxy phenol as inhibitor, polymerization of the solvent is avoided. In order to produce the precursor which is $PbTiOL_4$ (L is $[OOCC(CH_3)=CH_2]^-$), individual formation reactions of lead methacrylate and titanium propoxide methacrylate from lead oxide and titanium isopropoxide can be written as follows:

$$PbO + 2\,CH_2{=}C(CH_3)COOH \xrightarrow{\Delta / CHCl_3} Pb(OOCC(CH_3){=}CH_2)_2 + H_2O$$

Equation 3.1 Precursor – Lead alkoxide

$$Ti(OC_3H_7)_4 + 2CH_2{=}C(CH_3)COOH \xrightarrow{\Delta / CHCl_3} Ti(OC_3H_7)_2(OOCC(CH_3){=}CH_2)_2 + 2\,C_3H_7OH$$

Equation 3.2 Precursor – Titanium alkoxide

Overall precursor reaction occurs in the presence of both lead oxide and titanium isopropoxide with methacrylic acid in reaction media. Note that water is added to complete the partial ligand exchange stoichiometry for titanium alkoxide and the solvent used as reaction media was chloroform (boiling point: 61°C) which was removed by rotary evaporation later on.

$$Pb(OOCC(CH_3){=}CH_2)_2 + Ti(OC_3H_7)_2(OOCC(CH_3){=}CH_2)_2 \xrightarrow{\Delta / CHCl_3} PbTi(OC_3H_7)_2(OOCC(CH_3){=}CH_2)_4 \quad (\textit{Intermediate-product})$$

$$PbTi(OC_3H_7)_2(OOCC(CH_3){=}CH_2)_2 + H_2O \xrightarrow{\Delta / CHCl_3} \mathbf{PbTiO(OOCC(CH_3){=}CH_2)_4} + 4\,C_3H_7OH$$

Equation 3.3 Overall Precursor Reaction

The solid precursor was placed in an oven for 2 days at 70°C for further drying and grinded to fine powder for calcinations use.

3.3.2 Polymerization and Pyrolysis.

The ligand in the precursor contains C=C double bond which enables polymerization of the amorphous precursor when it is thermally treated. Due to organic characteristics of the ligand, further calcination results in pyrolysis of the metaloxide by releasing the organic ingredients.

Experimentally, powder precursor is grinded well and placed in a crucible and heated in an owen. Combined polymerisation and pyrolysis take place as follow [44]:

$$n\ PbTiO(OOCC(CH_3)=CH_2)_4 \xrightarrow{\Delta} [PbTiO(OOCC(CH_3)=CH_2)_4]_n$$

Equation 3.4 Polymerization of the Precursor

$$[PbTiO(OOCC(CH_3)=CH_2)_4]_n \xrightarrow{\Delta} PbCO_3 + TiO_2 + C + volatiles$$
$$PbCO_3 + TiO_2 + C + volatiles \xrightarrow{\Delta} \mathbf{PbTiO_3} + CO_2$$

Equation 3.5 Pyrolysis and $PbTiO_3$ formation

The polymerization reactions shown in equation 3.4 occurs approximately 165°C. On the other hand, pyrolysis occurs at comparatively elevated temperatures. Completion of the reaction and evaporation of the organics is a matter of temperature and annealing time. It occurs around 340°C – 350°C band when it is calcined for 6 hours. This is the range that unit cell formation can be detected via EPR. Significant nucleation and growth of $PbTiO_3$ lattices start at about 385°C which can be detected via XRD and Raman.

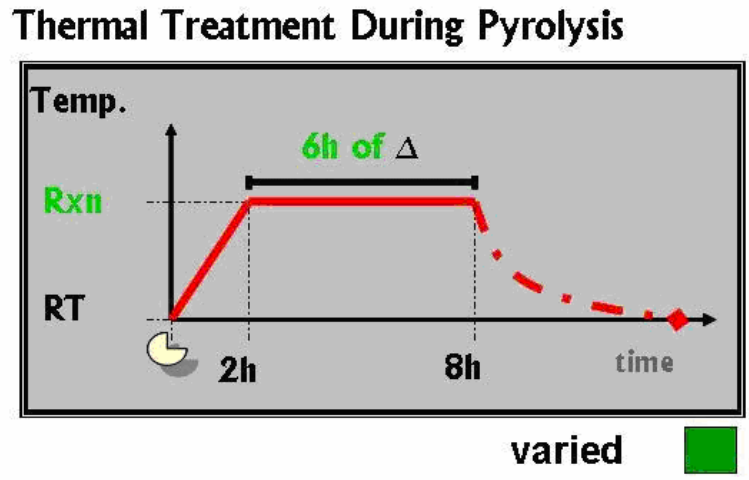

Figure 3.1 Calcination Scheme

In figure 3.1, the scheme represents thermal treatment applied during pyrolysis step. Calcination time plays significant role upon the mean particle size of the $PbTiO_3$ nanaocrystals. The longer the reaction takes place, the greater the mean particle size grows. However, when the reaction time is kept too short, the overall pyrolysis could be

incomplete. Typically, the samples were heated upto target temperatures in 2 hours and annealed for 6 hours at that temperature.

During this study, varied annealing temperatures are experimented in order to follow the unit cell formation and particle size of the $PbTiO_3$. The lowest calcination temperature examined is 300°C which is even lower than the completion of pyrolysis and taken as reference for an incomplete product. The most elevated calcination is done at 900°C which yields macro-size $PbTiO_3$ particles. Between 300°C – 400°C range, almost every 10°C incremented samples are synthesized while 400°C – 900°C range is sampled in every 50°C increments. Additional trials are added or reproduced in case of necessity and further examination to check the reproducibility.

Not only the reaction temperatures, but also the reaction time is also varied to optimize the reaction conditions yielding nanosize $PbTiO_3$ crystals. Several trials are annealed at the same temperature but for different calcination durations such as 3 hours, 6 hours, 12 hours and 18 hours to check the crystal formation and particle growth.

Further manipulations to reduce the particle size are done by using well known ball milling technique.

Table 3.2 List of experimental trials

	3h	6h	12h	18h		3h	6h	12h	18h
300°C		+			**450°C**		++		++
330°C		+		+	**500°C**		+		
340°C	++	++	++	++	**550°C**		+		
350°C		+		+	**600°C**		+		
360°C		+			**650°C**		+		
370°C	+	+	+	+	**700°C**		+		
375°C		++			**720°C**		+		
380°C		+			**750°C**		+		
390°C		+			**800°C**		+		
400°C		+			**850°C**		++		
420°C		++			**900°C**		+		

+ Synthesized. **++** Synthesized and ball milled.

3.4 Post Synthesis Treatment

When the calcination step was done the samples were collected and prepared for further characterization. The main step to decrease the grain size of the crystals is ball milling. Most of the samples are soft milled in different time intervals starting from 5 minutes to 1 day (mostly 5 minutes, 10 minutes, 20 minutes, 30 minutes, 40 minutes, 1 hour, 6 hours and 24 hours). 1 gram of relevant sample is placed in the milling chamber which is made of steel and contains several spherical balls. The main principle of the ball milling is based on the collision kinetics of the moving parts and the sample. Each collision presses the compound and forces the unit cell to reshape while transferring their energy.

After the milling step, most of the sample is sticked to the inner walls or the balls of the chamber so, scrapping the powder is required to gain the yield.

Both pyrolized and ball milled samples become ready to be characterized via previously stated methods.

Chapter 4

Results, Analysis and Discussion

4.1 Experimental Observations

All reactants were well grinded and stoichiometrically mixed, prior to use. The reflux system consisted of three-necked round bottom flask equipped with thermometer and a plastic stopper for water injection. Three hours of reflux period started at 61°C, which is the boiling point of chloroform. Light yellow / cream color of the suspension can be taken as indication of the precursor formation. After three hours, chloroform is removed from the system via rotary evaporator. Mud like solid is dried for 48 hours at 70°C. When the drying step is completed, the precursor is finely grinned in a mortar for further CPP processes.

When the precursor is heated up to elevated temperatures, metallorganic precursor turns into metaloxide by releasing the organic ingredients. Evaporation of the organics causes sharp, harmful stink even the oven is placed in the hood. Completion of the pyrolysis is indicated via the removal of black color of the sample coming from the carbon including organic byproducts. Color change of the precursor from light cream to black in 300°C – 330°C band proves this phenomenon.

At higher calcinations temperatures, the grain size of the $PbTiO_3$ crystals is also increased. Observations show that with respect to the grain size, a slight color change occurs because particle size affects the diffuse reflectance of the light. Figure 4.1 shows the pictures and corresponding colors of the $PbTiO_3$ samples which are calcined at different temperatures.

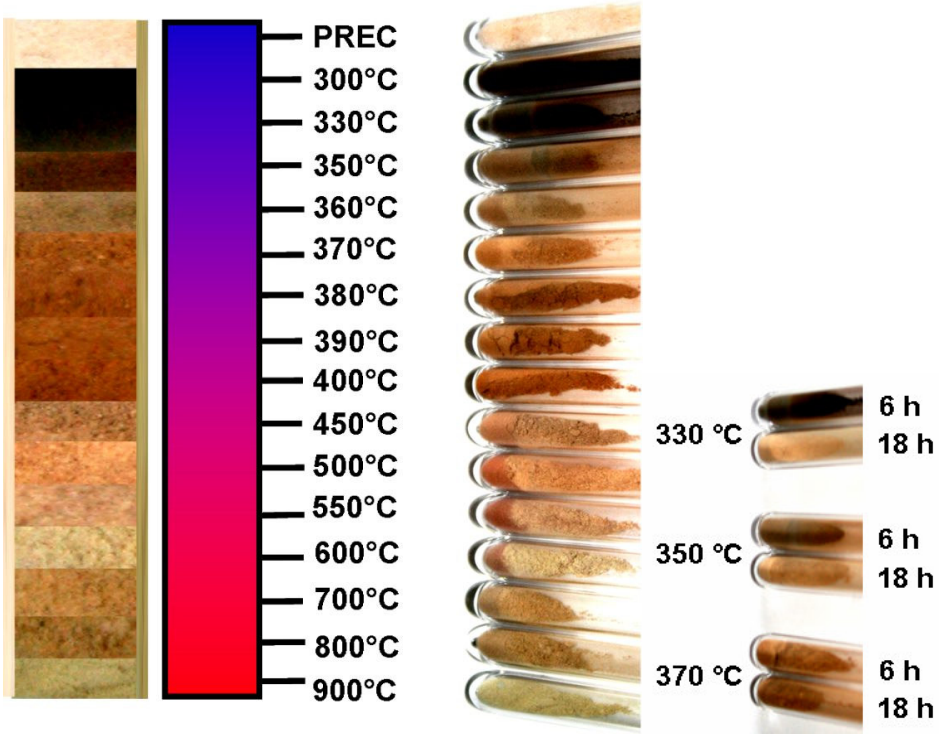

Figure 4.1 Colors of $PbTiO_3$ prepared at different temperatures

4.2 TG / DTA Analysis

As previously introduced, TG / DTA is a significant method of measuring weight loss of a sample as a function of time. This characterization gives information about the reaction temperature, yield ratio, phase changes, according to the weight loss and energy difference calculations. The measurement media can be adjusted (under air, N_2, etc). In this study, measurement is done under air like all calcinations. 200ml / min air flow is adjusted by the analyzer. Sample is put into a platinum crucible. 15.5 mg is sample is analyzed. Since the released gasses are harmful, a funnel set is used for the reaction atmosphere transfer from the analyzer to the hood.

Table 4.1 TG /DTA Temperature Program

	$°C_i$	$°C_f$	°C / min	min	s
1	**25**	**550**	**10**	**0**	**0.5**
2	**550**	**25**	**10**	**0**	**0.5**

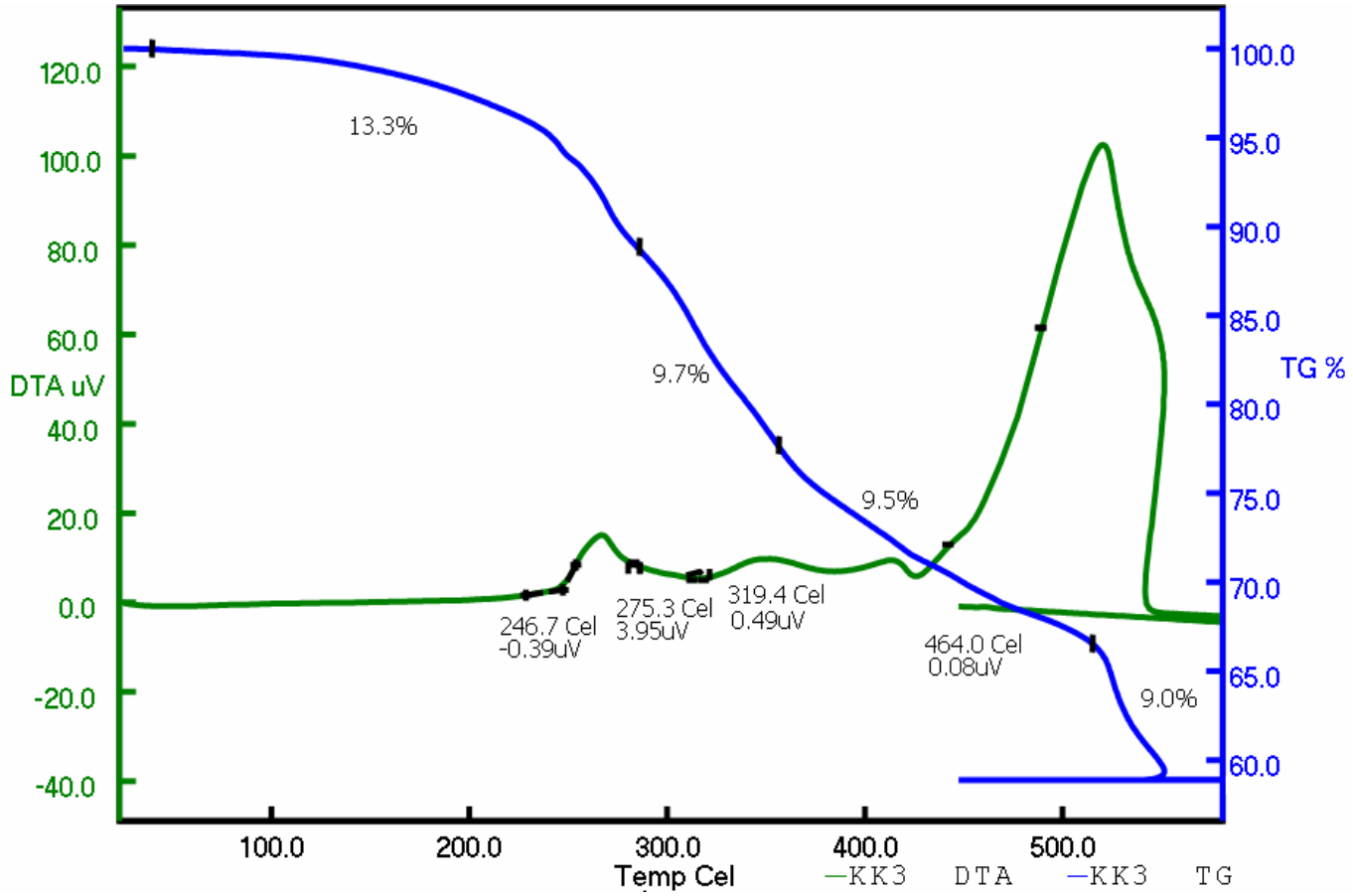

Figure 4.2 TG/DTA Analysis of $PbTiO_3$ Precursor

Figure 4.2 shows the results of the TG (green – weight loss) and DTA (blue – thermal change) measurements. The blue line representing the TGA curve of the precursor reveal characteristic thermal effects due to CPP formation reactions, evaporation of volatiles or phase change of the crystal.

As CPP reactions previously explained in detail, the temperature changes starting from 245°C to 345°C region is due to the polymerization of the precursor and the pyrolysis of the metallorganic precursor to metal oxide.

As can be seen from the weight loss data, almost half of the reactant mass is lost during the heating process which can be explained with the evaporation of the organic ligands during the pyrolysis step. However, the TG results for the weight loss do not

perfectly match with the reaction stoichiometry. According to the previous studies, intermediate-products (organometallic compound with the alkoxide ligands and methacrylate ligands) make substitution reaction during precursor synthesis [43]. The substitution can be done from 1 – 6 (6 because Pb and Ti has overall +6 charge while the ligands both have -1 charge) different ligands range which is accepted as 4 substitutions in our precursors case due to the nature of the perovskitic compound. However, since it is an ongoing reaction and the precursor is an intermediate-product on this series, the exact substitution order can not perfectly be defined. Moreover, the excess PbO also causes an alteration on the gravimetric calculations which is added to avoid the reactant loss due to the evaporation of lead oxide.

Around 490°C which is the *Curie Temperature* of the $PbTiO_3$, phase transition occurs from tetragonal phase to cubic phase so the DTA respond occurs in this region. Phase transition is also verified via EPR results exactly in this temperature which will be examined in upcoming sections. Unit cell alteration in the piezoelectric and ferroelectric crystals also changes the physical, chemical and electrical properties of the material, such as dielectric constant and dimensions of the unit cell [43].

4.3 X – Ray Diffraction Analysis

Among numerous benefits of X – Ray Diffraction technique, structure confirmation becomes the first and most significant one. By comparing the data with the crystal library references which is formed throughout the science history, structure verification can be done. Particle size calculations are also done via XRD results.
In figure 4.3, upper red line belongs to the XRD data of $PbTiO_3$ prepared at 900°C and it is compared to the literature values at the bottom with black line that are taken from Inorganic Crystal Structure Database (ICSD). Symmetry group is assigned as P4/mmm and the dimensions of unit cell is calculated as a = 3,89Å and c = 4,15Å while c/a = 1,06. On the other hand, the comparison of the $PbTiO_3$ sample prepared in 800°C via CPP route (top) and amorphous precursor (bottom) can be seen in figure 4.4. The indexed reflection indicate the formation of single phase tetragonal $PbTiO_3$.

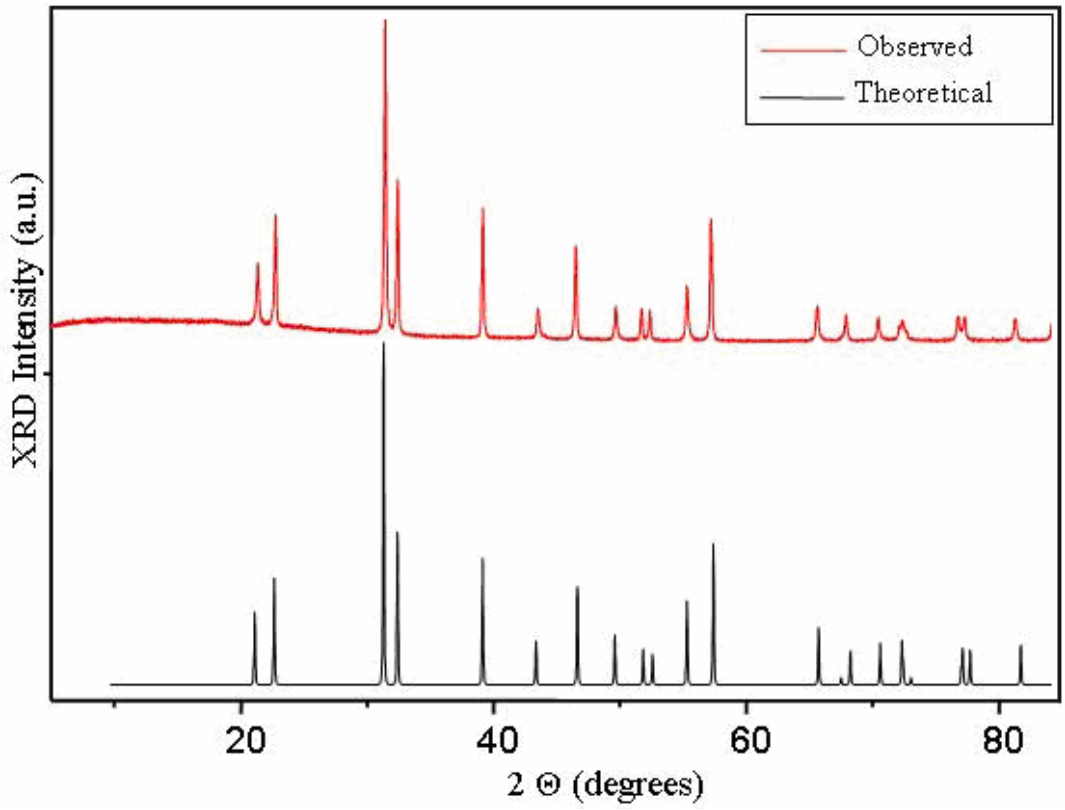

Figure 4.3 XRD confirmation of $PbTiO_3$

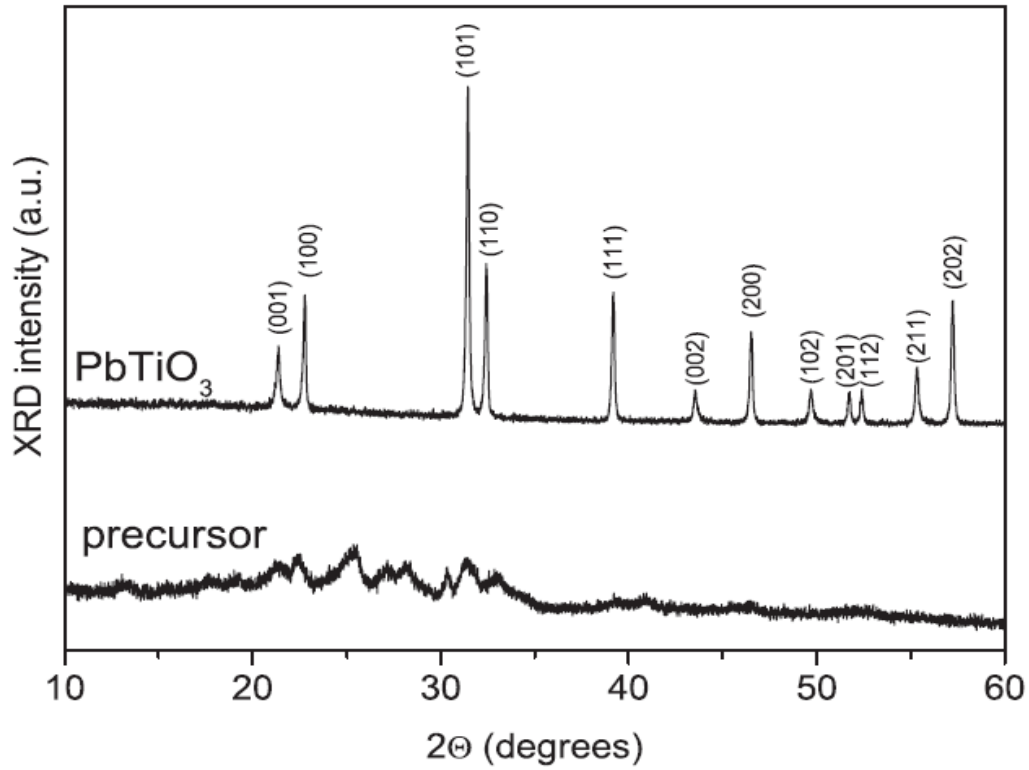

Figure 4.4 Powder diagram of $PbTiO_3$ prepared by CPP route.

Crystal data of the tetragonal $PbTiO_3$ is literated exactly as [46]:

[70-746] PDF-2 Sets 1-86 Quality: C Wavelength: 1.540598 .

Lead Titanium Oxide - Pb Ti O_3

Rad.: CuKa1 (1.54060) Filter: d-sp: calculated
I/Icor.:11.74 Cutoff: 17.7 Int.: calculated
Ref.: Calculated from ICSD using POWD-12++, (1997)

Sys : Tetragonal S.G. : P4mm (99) V(redu): 63.3
a: 3.90500 b: c: 4.15600 C: 1.0643
A: B: C: Z: 1 mp:
Dx: 7.940 Dm: SS/FOM: F26= 999.9 (.0001, 26) ICSD: 001612
Ref.: Glazer, A.M., Mabud, S.A., Acta Crystallogr., Sec. B, 34, (1978), 1065

ea: nwB: ey: Sign: 2V: .

REM TEM 298. // At least one TF implausible.

Hanawalt: 2.85/G 2.76/G 3.91/G 2.30/G 1.61/G 1.95/G 4.16/G 1.66/G 2.08/G 1.83/G
Max-d: 4.16/G 3.91/G 2.85/G 2.76/G 2.30/G 2.08/G 1.95/G 1.83/G 1.77/8 1.75/7

d[A]	2Theta	Int.	h k l	d[A]	2Theta	Int.	h k l
4.1560	21.363	242	0 0 1	1.3369	70.363	64	2 1 2
3.9050	22.754	361	1 0 0	1.3102	72.018	26	2 2 1
2.8458	31.409	999	1 0 1	1.3056	72.313	67	1 0 3
2.7613	32.397	451	1 1 0	1.3017	72.566	40	3 0 0
2.2999	39.136	336	1 1 1	1.2422	76.650	55	3 0 1
2.0780	43.517	109	0 0 2	1.2382	76.939	36	1 1 3
1.9525	46.472	243	2 0 0	1.2349	77.187	61	3 1 0
1.8344	49.658	108	1 0 2	1.1837	81.195	51	3 1 1
1.7672	51.684	77	2 0 1	1.1500	84.112	44	2 2 2
1.7464	52.346	67	2 1 0	1.1298	85.966	19	2 0 3
1.6604	55.283	172	1 1 2	1.1031	88.581	15	3 0 2
1.6100	57.168	306	2 1 1				
1.4229	65.551	105	2 0 2				
1.3853	67.565	12	0 0 3				
1.3806	67.826	63	2 2 0				

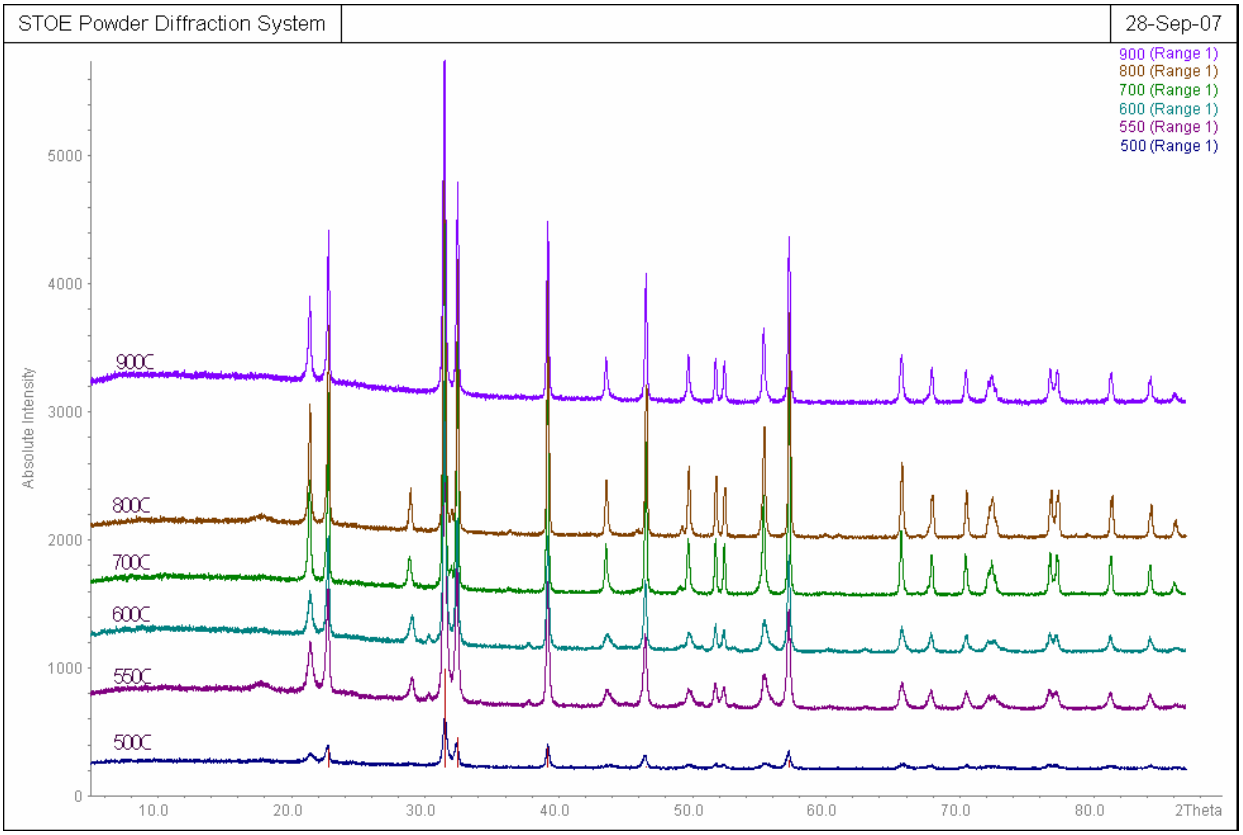

Figure 4.5 XRD of 500°C – 900°C $PbTiO_3$ samples

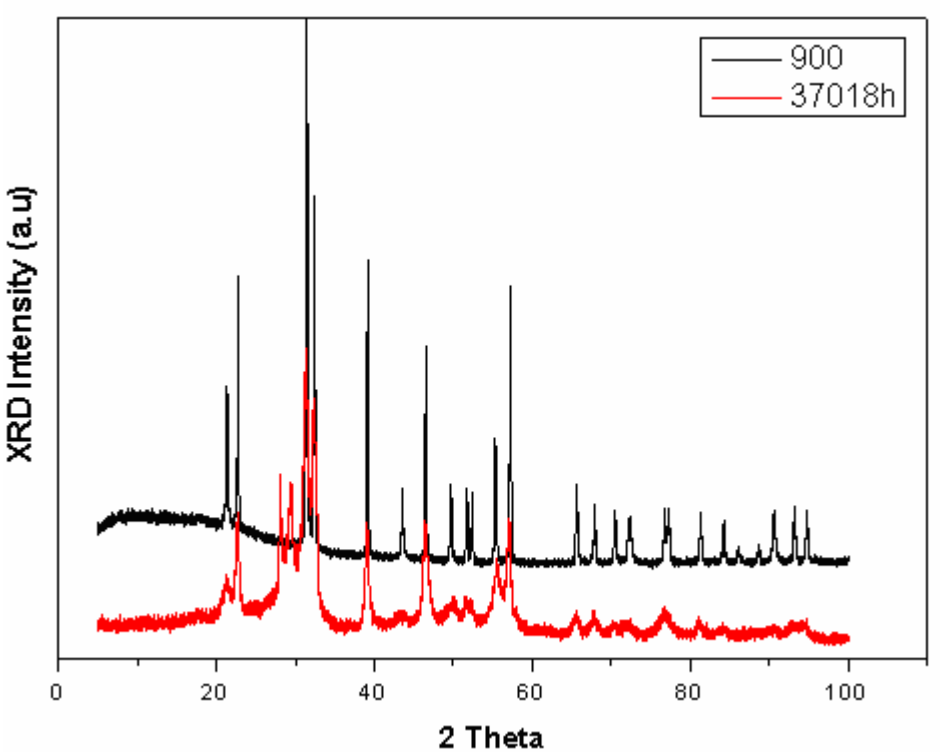

Figure 4.6 Beginning of the $PbTiO_3$ crystal formation.

In figure 4.5, the samples prepared between 500°C – 900°C range can be viewed. The unit cell formation of the $PbTiO_3$ crystal starts around 350°C region, however, the XRD and Raman are not able of detecting this "short range" order. For instance, figure 4.6 compares two diffraction spectrums: The upper one belongs to 900°C – 3 hour calcined $PbTiO_3$ and the lower one belongs to 370°C – 18 hours calcined sample. Crystal formation starts around 370°C, however, regular 6 hours of calcination may not be enough for formation kinetics especially for lower temperatures. So, the data is taken from the sample prepared in 18 hours of annealing. However, it is still not as clear crystalline as the 900°C sample and information is hardly noticed out of the noise due to the weak intensity.

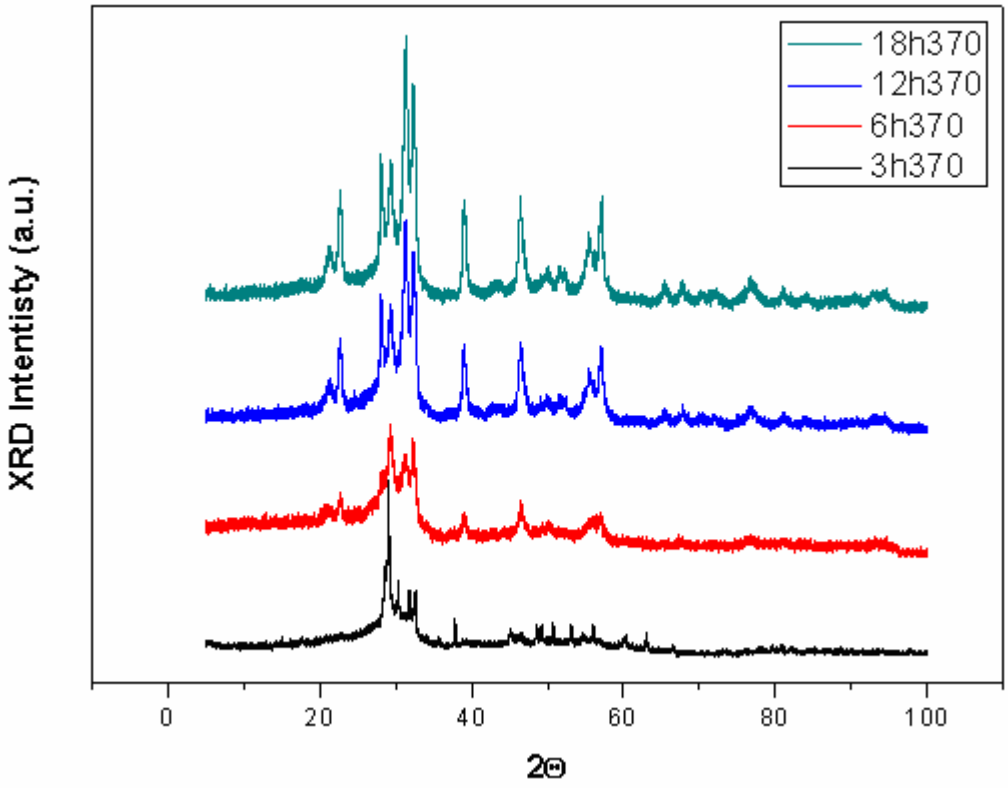

Figure 4.7 Comparison of different calcinations times

In figure 4.7, different calcination times of the same temperature can be seen. All four precursors reacted at 370°C but the reaction time varies 3 hours, 6 hours, 12 hours and 18 hours from bottom to top. The formation of the crystal lattice can be seen from the more intense peak formation.

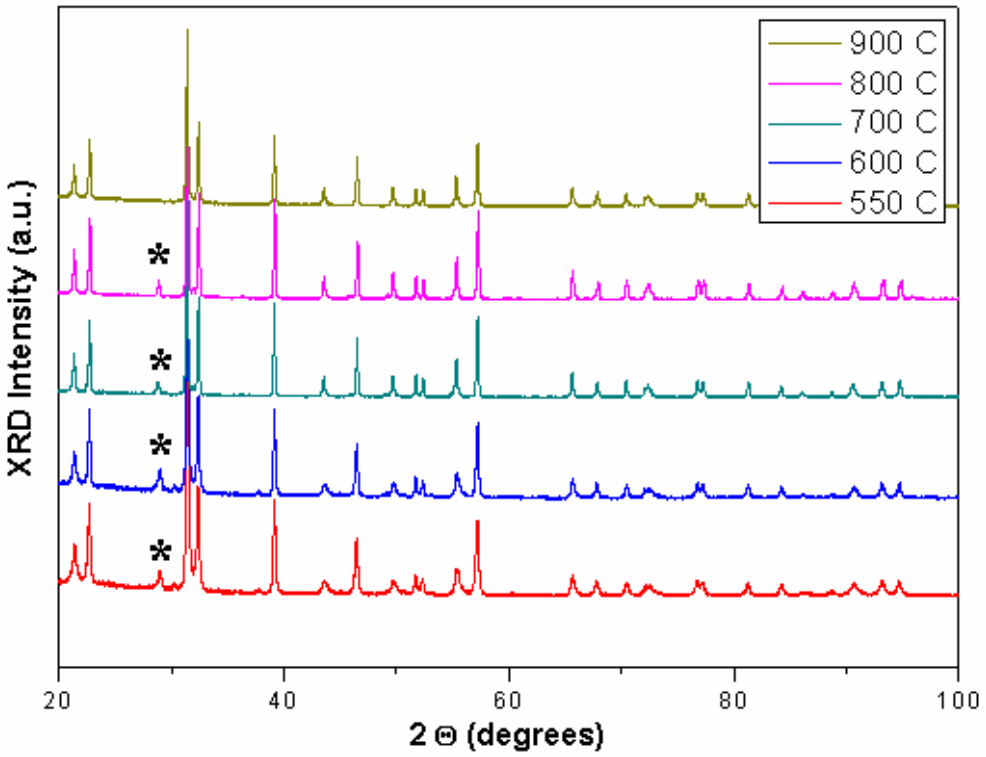

Figure 4.8 Existence and evaporation of PbO

According to Inorganic Crystal Structure Database, pure lead oxide give two close signals around 28° and 29.5° 2Θ degrees, which can easily be detected as an additional signal to the $PbTiO_3$ in most of the samples due to the excess lead oxide in reactants. The signal around 30° disappears indicating the evaporation of PbO at 900°C which is over the melting point (888°C) of PbO.

Table 4.2 Particle size calculations

Sample	2 Θ	Size (nm)
900°C	31,455	**384,48**
800°C	31,470	**343,77**
700°C	31,449	**212,50**
600°C	31,450	**104,43**
550°C	31,460	**70,51**
500°C	31,495	**40,05**
450°C	31,520	**32,36**
400°C	31,435	**18,96**
390°C	31,375	**14,25**
380°C	31,351	**13,77**
370°C	29,375	**13,05**
350 °C 18h	29,375	**10,77**

The particle size was determined using Scherrer's equation $D = k \lambda / \beta \cos(\theta)$ where D is the mean grain size, k the Scherrer's constant (k = 0.9 for FWHM), λ the X-ray wavelength, β the full width at half maximum (FWHM) of a diffraction peak, and θ the diffraction angle. Sherrer – equation is used to calculate the grain size of the crystals. Full width at half maximum rule is used for these calculations. Although the samples prepared at lower temperatures have weaker signal to noise ratio, rough calculations are done in order to see the relative particle size change by reducing the preparation temperature as in table 4.2. Note that, by using CPP route and altering the calcination temperature, grain size can be shifted from micron scale to nano scale while reducing temperature.

4.4 Raman Results

In addition to XRD analysis, Raman scattering is the second method that we benefited to confirm the crystal structure and the structural changes. By subsequently using Raman spectroscopy, it is also possible to account for the expected softmode behavior of ferroelectric $PbTiO_3$ particles. The soft mode E(1TO) is a prerequisite for the existence of long-range phenomena and often is used as a fingerprint for the existence of ferroelectricity. The corresponding spectra are displayed in figure 4.9.[38]

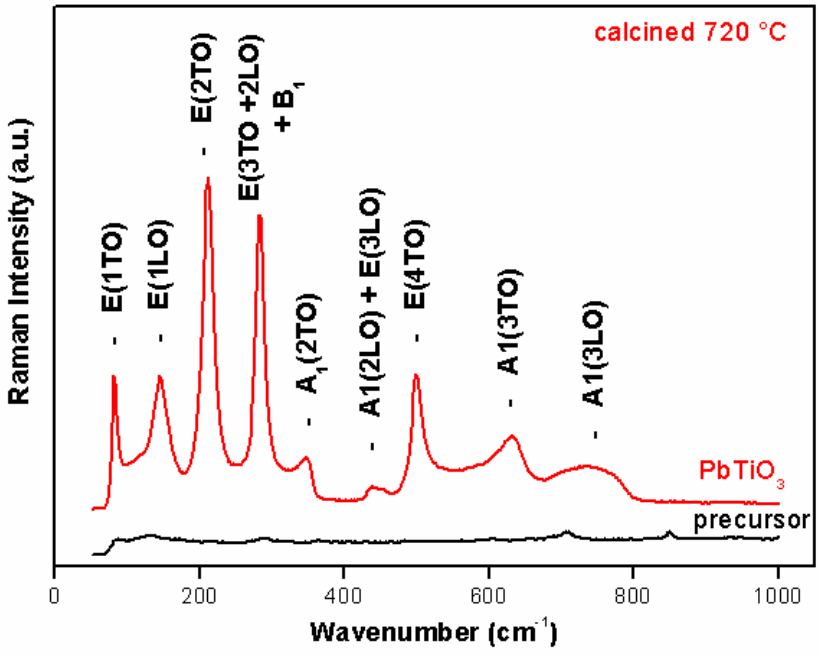

Figure 4.9 Raman confirmation of $PbTiO_3$

For a sample calcined at 720°C, all expected Raman-active modes for $PbTiO_3$ [47] were observed. As compared to the Raman frequencies reported for 'pure' $PbTiO_3$ no significant shifts could be registered for the Fe^{3+}- modified $PbTiO_3$ compounds. On the other hand, for the amorphous precursor, no significant Raman-active modes could be detected at all.

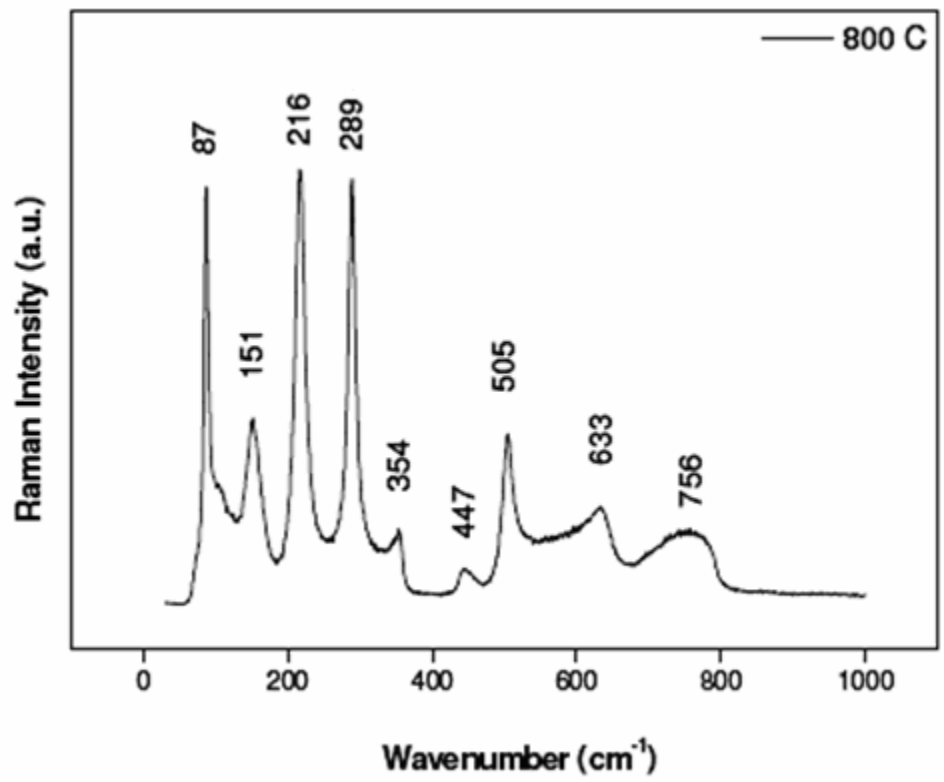

Figure 4.10 Raman spectra of the sample synthesized at 800°C

Exact wavenumbers corresponding to Raman modes can be seen on the spectra of the sample that is calcined at 800°C in figure 4.10. Except the mode around 290cm^{-1} which is literated as silent mode and shows no change with respect to the particle size, [48] other modes show broadening and relative shifts [49].

Table 4.3 Corresponding wavenumbers of the active modes (800°C sample)

E(1TO)	E(1LO)	E(2TO)	E(3TO+2LO)+B1	A_1(2TO)
86,9 cm^{-1}	151,1cm^{-1}	216,0 cm^{-1}	288,7 cm^{-1}	353,5 cm^{-1}

A_1(2LO)+E(3LO)	E(4TO)	A_1(3TO)	A_1(3LO)
446,8 cm^{-1}	505,0 cm^{-1}	632,8 cm^{-1}	756,4 cm^{-1}

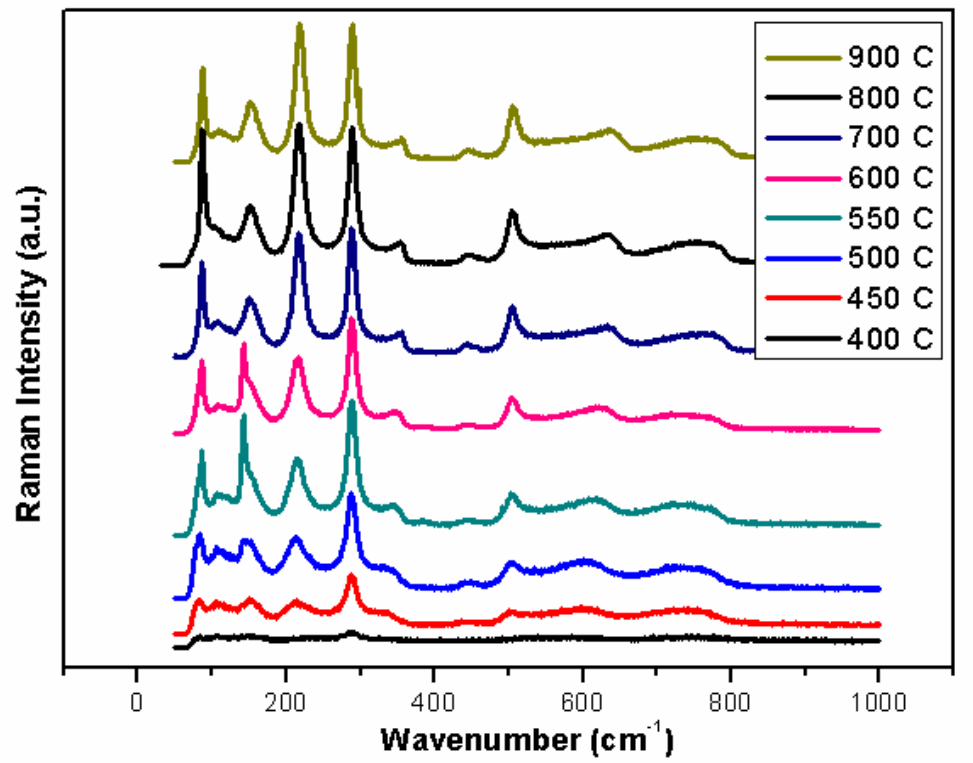

Figure 4.11 Raman spectrum for 400°C – 900°C samples

Development of the crystallization can be seen from the formation of qualitatively better spectra while the calcination temperature increases as in figure 4.11. Moreover, from the most informative soft mode, E(1TO) around 90 cm^{-1}, we can conclude that the higher calcination temperature is, the sharper soft mode detected. It is due to the development of the tetragonal structure of $PbTiO_3$ while lattices host more ferroelectric unit cells.

As previously mentioned, Raman scattering is not a highly sensitive and efficient method, thus, samples which are synthesized at lower temperatures could not crystallized well enough to be detected via Raman scattering. Figure 4.12 is a good example to visualize the crystallization completion for various temperatures. The bottom spectrum belongs to 330°C trial and although it is thermally treated for 18 hours (which is triple of the default calcinations time), the temperature is not high enough to form $PbTiO_3$ crystals. The spectrum belonging to 720°C experiment is given as crystalline reference and the top spectrum tagging sample annealed at 350°C for 18 hours sample shows the start of the long range order in the structure. Especially soft modes can be separated from baseline.

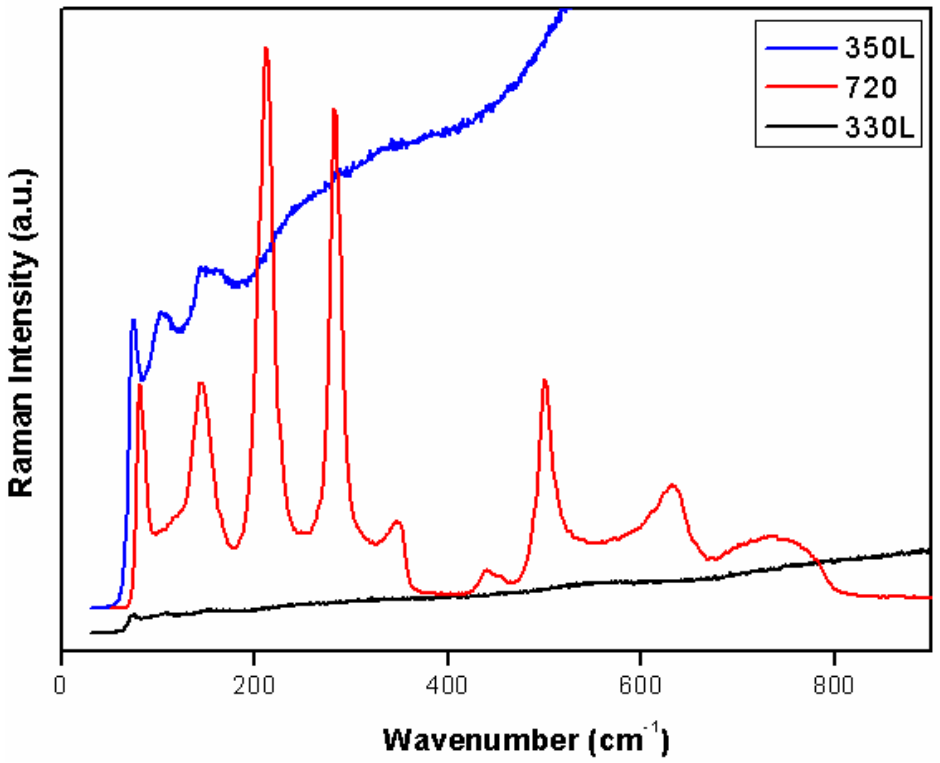

Figure 4.12 Raman spectrum for lower temperatures in $PbTiO_3$ synthesis

4.5 Electron Paramagnetic Resonance Analysis

EPR is a spectroscopic technique that detects unpaired electrons' spin, identity of the molecule, information of the molecular structure and the molecular environment. Specifically, EPR technique plays a key role in our study to examine the changes in the unit cell formation, with respect to experimental treatments.

For numerical spectrum analysis of the EPR data, the free trivalent iron ion is considered as possessing five unpaired electrons in the 3d shell ($3d^5$) with a high-spin $^6S_{5/2}$ ground state (S = 5/2). It was recently reported that acceptor-type centers form defect dipoles with charge-compensating oxygen vacancies, such as $(Fe'_{Ti,Zr} - V_O^{\bullet\bullet})^{\bullet}$ [50,51] or $(Cu'_{Ti,Zr} - V_O^{\bullet\bullet})^{\bullet}$ [52] in $Pb[Zr_xTi_{1-x}]O_3$ (PZT) [53].

Concerning the $(Fe'_{Ti,Zr} - V_O^{\bullet\bullet})^{\bullet}$ defect dipoles, the orientation of the dipole with respect to one of the spontaneous polarization is a function of crystal symmetry and lattice distortion [54, 55]. Therefore, a marked effect on the formation and orientation of

$(Fe_{Ti}^{'} - V_O^{\bullet\bullet})^{\bullet}$ defect dipoles is expected for $PbTiO_3$ nanocrystals. In this part of the work, we therefore aim to synthesize and systematically study the interplay between grain size and characteristics of $(Fe_{Ti}^{'} - V_O^{\bullet\bullet})^{\bullet}$ defect dipoles in Fe^{3+}-modified $PbTiO_3$ nanocrystals.

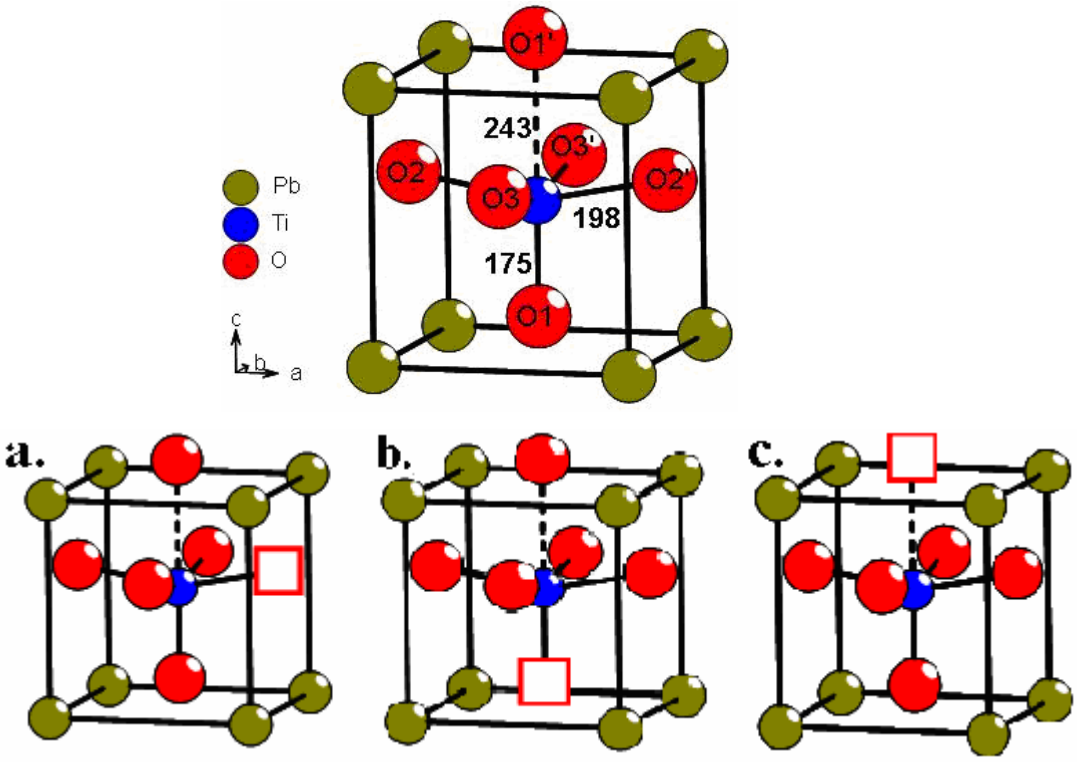

Figure 4.13 Charge compensation by neighbouring oxygen vacancies in $PbTiO_3$

Two major information can be obtained by using EPR technique: firstly, the difference between isolated $Fe_{Ti}^{''}$ center and compensated by charge $(Fe_{Ti}^{'} - V_O^{\bullet\bullet})^{\bullet}$ defect dipole can be distinguished and secondly, the site symmetry at the Fe^{3+} - site can be obtained. The defect dipoles may be oriented either perpendicular $(Fe_{Ti}^{'} - V_O^{\bullet\bullet})^{\bullet}_{\perp}$ as in figure 4.13.a or parallel $(Fe_{Ti}^{'} - V_O^{\bullet\bullet})^{\bullet}_{//}$ as in figure 4.13.b with respect to the orientation of unit cell polarization.[53] In case of an 'isolated' $Fe_{Ti}^{''}$ center, an isotropic EPR line indicates cubic $PbTiO_3$ phase [56]. (-1) charge is favorable in comparison to (+2) thus oxygen vacancy is formed in order to compensate the overall charge at the unit cell. According to literature, Newman superposition model calculates which oxygen is more "willing" to be removed. 4 oxygen atoms on sides (O_2, $O_2^{'}$, O_3, $O_3^{'}$) has equal distance

with the center, while O_1' is more far and O_1 is closer to the dopant at the center. Calculations confirm predictions and closer oxygen at c – axis, O_1, is more favorable to be released [53].

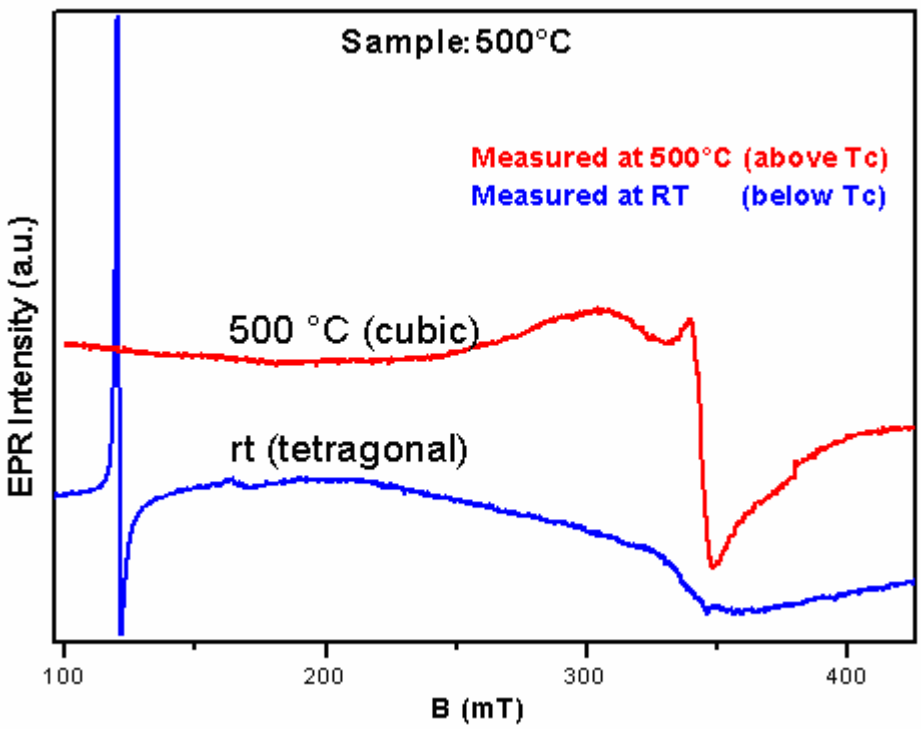

Figure 4.14 EPR of 500°C sample (top) above (bottom) below the Curie Temperature

As previously discussed, perovskitic $PbTiO_3$ calcined at elevated temperatures has tetragonal crystal structure which is dipolar and paramagnetic, however, when the sample is heated over its Curie Temperature (T_c), phase change occur and dimensions of the unit cell expand and structure transforms to cubic phase. Figure 4.14 shows the tetragonal samples' EPR measurements which are done above and below the T_c. This two signal become reference for us in order to define whether the crystal is tetragonal (tetr) or cubic. In addition to those phases, a rhombohedral (rhom) intermediate-phase is also seen.

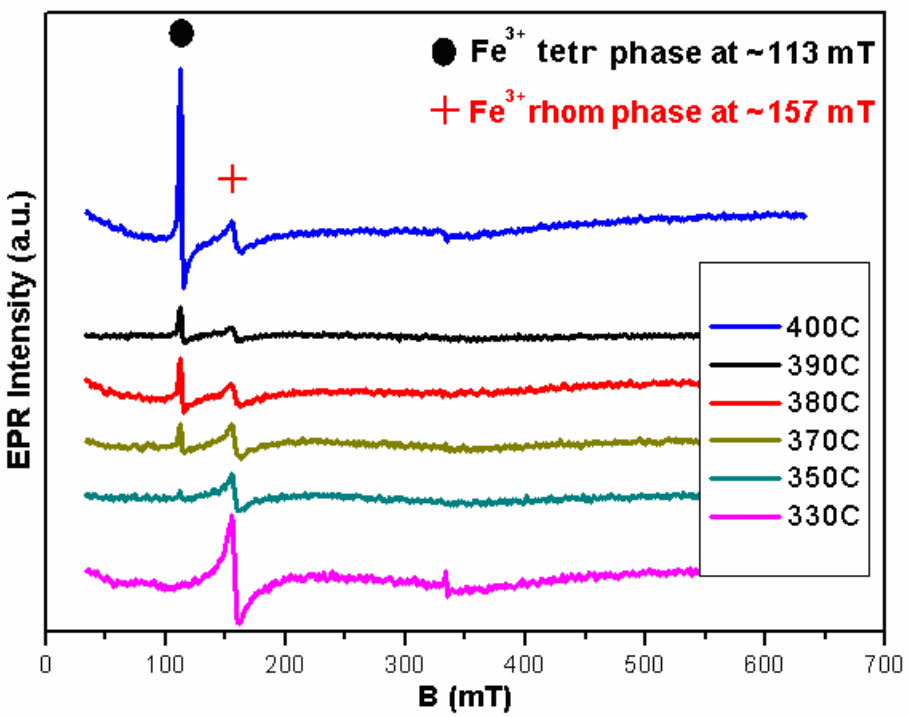

Figure 4.15 EPR analysis of 330°C – 400°C samples

The development of crystal structure from precursor to CPP synthesized $PbTiO_3$ samples occurs as in the order of amorphous from rhombohedral to tetragonal with respect to temperature increase. Cubic phase is not favored thermodynamically in this scenario. Cubic phase occurs only at elevated temperatures of $PbTiO_3$ nanocrystals. It is interesting to note that, carbon content in precursor is also EPR active showing a characteristic peak around 334 mT which is exactly at the same region of cubic $PbTiO_3$. However, carbon peak is much sharper and narrower due to its intensity and electron characteristics while cubic $PbTiO_3$ has relatively wider and symmetric peak. Best differentiation can be done by analyzing the integral of the EPR spectra, which is the raw data. In figure 4.16, all the samples are synthesized at 370°C but in different calcination times to examine the completion of reaction and unit cell alteration. Since the reaction is incomplete in 3 hours sample shown at the bottom, carbon existence generates sharp characteristic peak around 334 mT. Further calcinations (6 hours) proved to be sufficiently enough to remove the carbon content, while the unit cell formation is the mixture of both rhombohedral and tetragonal. Tetragonal phase is the thermally favored one and lattices are more ordered for longer durations.

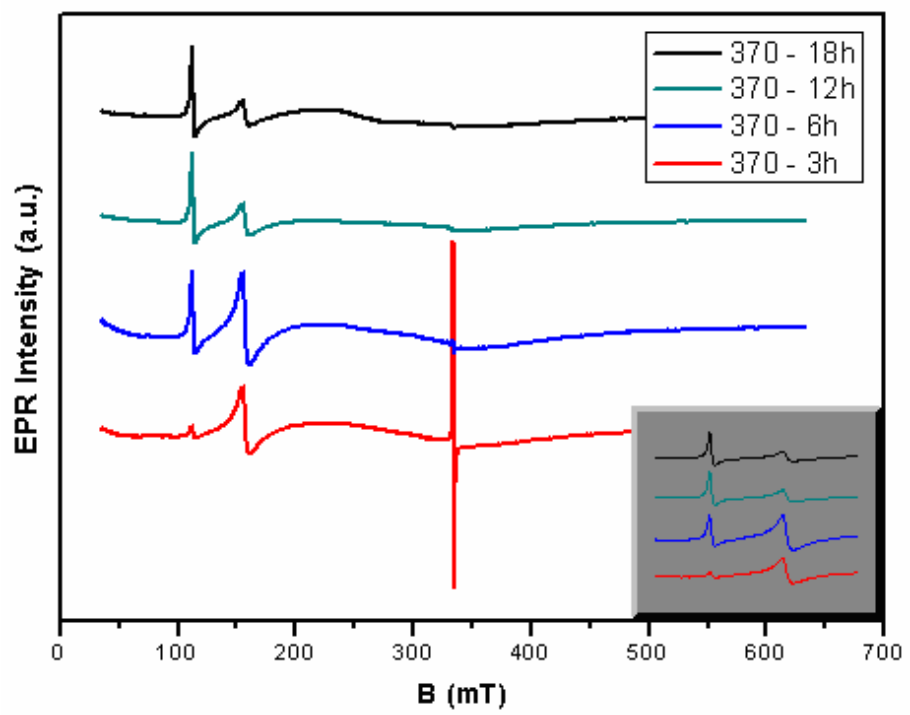

Figure 4.16 Time variation in the 370°C samples

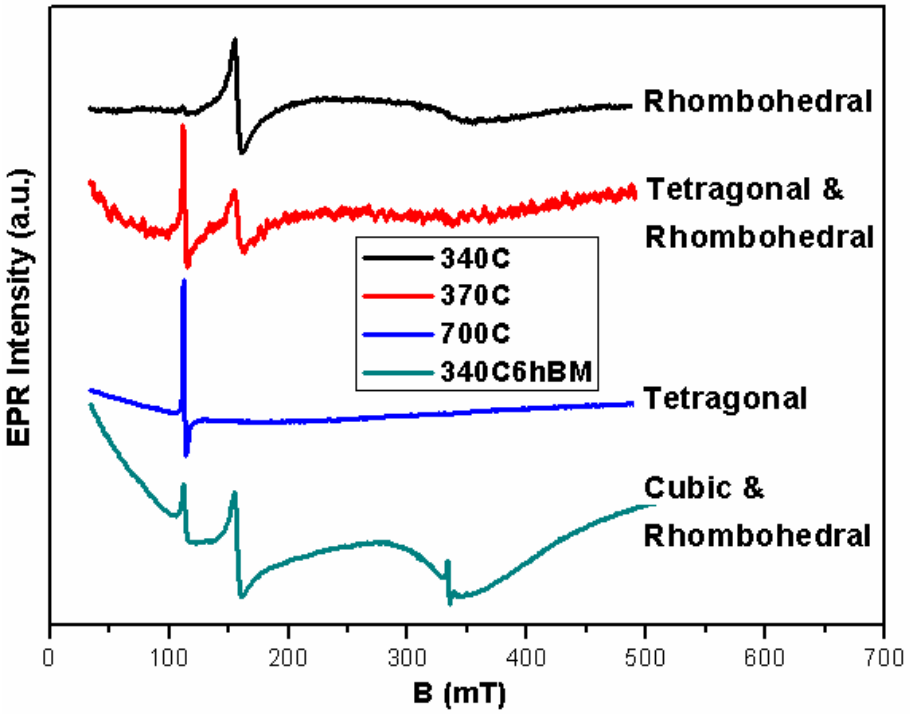

Figure 4.17 Different phases of $PbTiO_3$

To obtain size-driven tetragonal to cubic phase change, ball milling is used to manipulate the nanocrystalline samples. Below the critical size of nanoparticles, core shell model shows effect and extra tension of the grain boundary impacts the units in the shell and distorts the crystals in comparison to the ones in core. These factors drive crystal structure thru the cubic phase figure 4.18. Since the samples having lower calcination temperatures are not completely ordered, unit cells end up with smaller grain size. So, rhombohedral samples are easier to be manipulated to form the cubic structure.

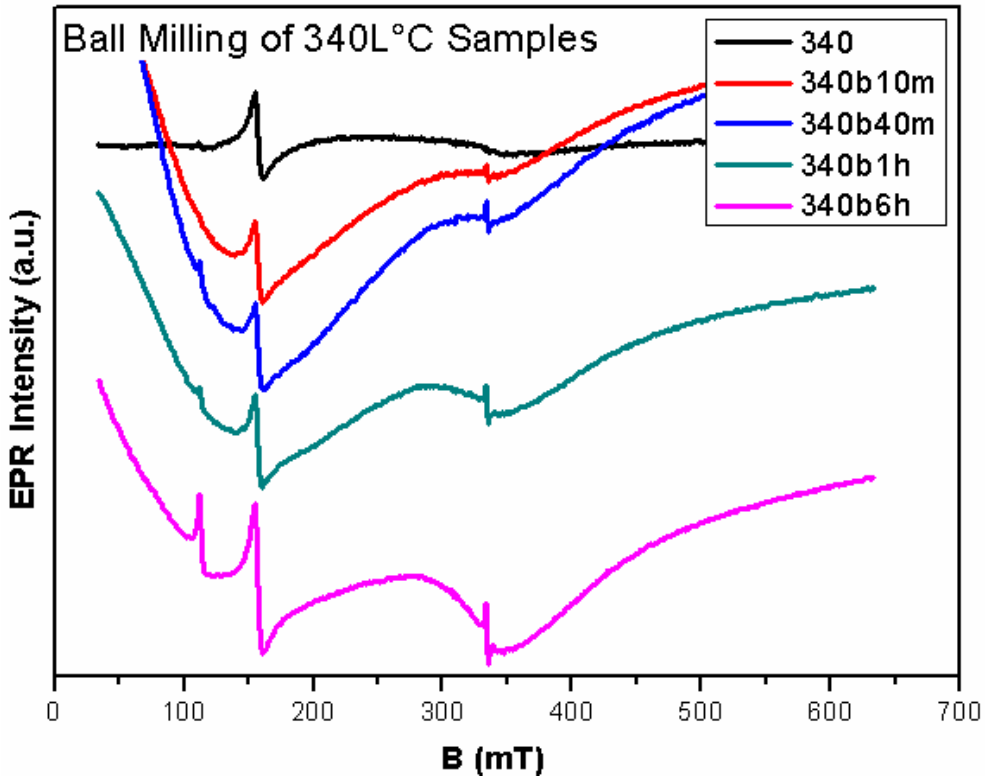

Figure 4.18 EPR of ball milled 340°C samples

As in figure 4.19 and figure 4.20, manipulation to the cubic cell formation becomes harder for larger molecules that are calcined at higher temperatures. That's why, the transformation of distorted rhombohedral cells are more favored.

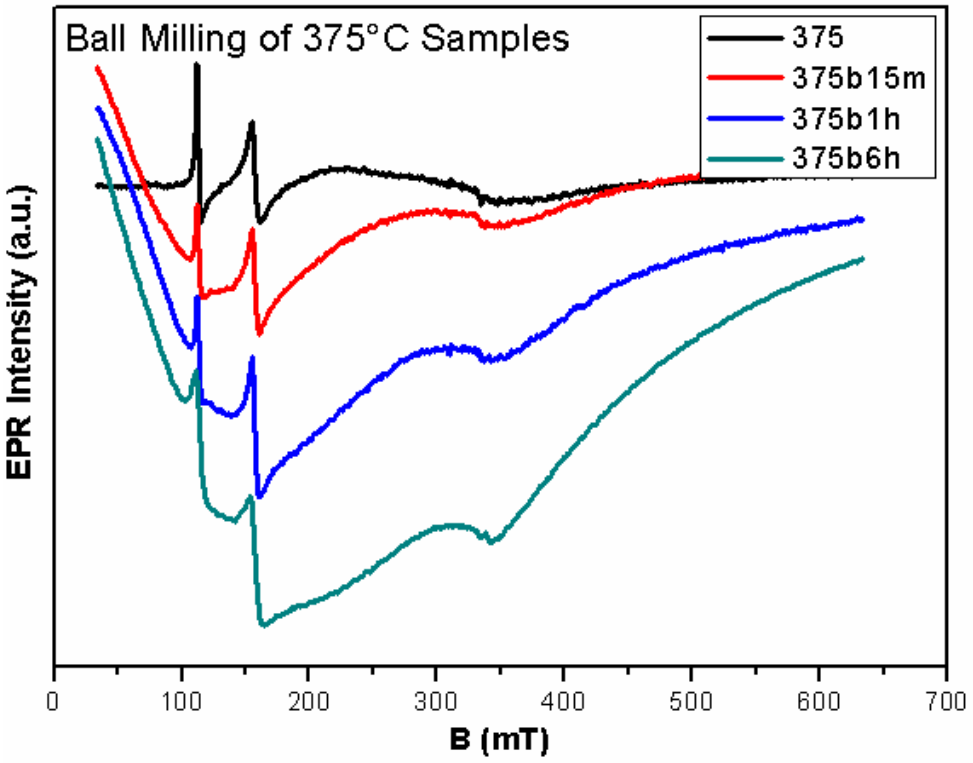

Figure 4.19 EPR of ball milled 375°C samples

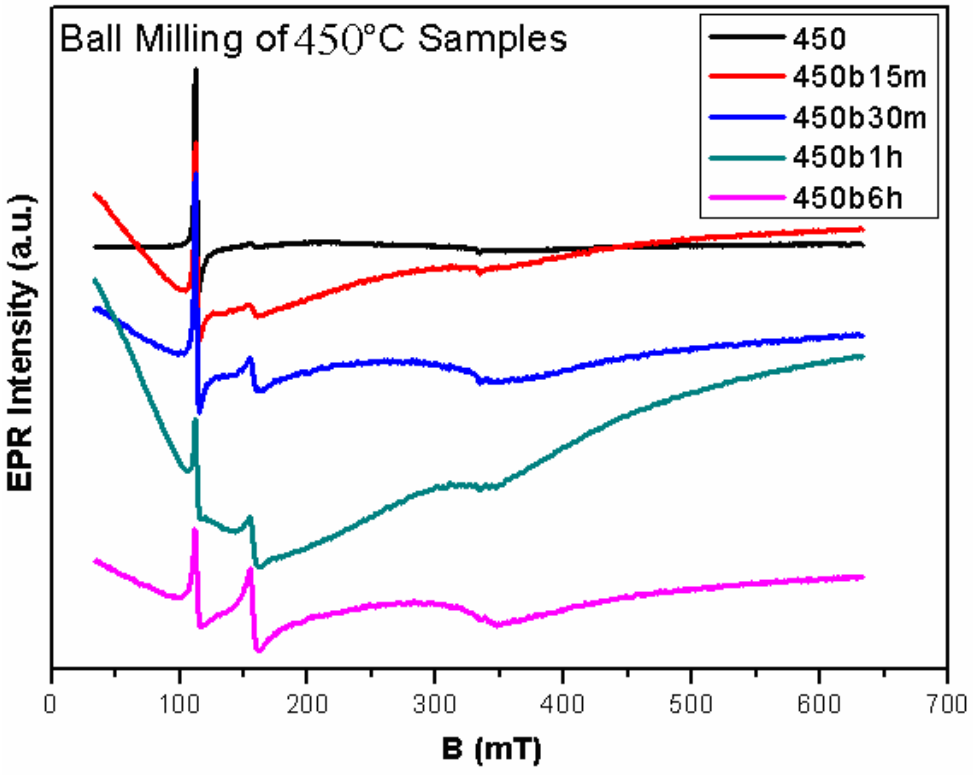

Figure 4.20 EPR of ball milled 450°C samples

Chapter 5

Conclusion

Lead titanate, $PbTiO_3$, is one of the most advanced metal oxide ceramics showing functional characteristic properties such as ferroelectricity, piezoelectricity and pyroelectricity. It is usually prepared by the solid state reaction of the binary oxide PbO and TiO_2 or $Ti(OR)_4$ molar ratio 1:1 at elevated temperatures.

In this study, the synthesis of Fe^{3+}-modified $PbTiO_3$ nanopowders has been experimented by using the CPP (combined polymerization and pyrolysis) for the first time. Reaction temperature was reduced till the 300°C – 400°C range which is much lower than employed for the conventional synthesis methods. Thermal treatment (calcination temperature and duration) during CPP affects significantly the grain size of the crystals. The temperature range between 300°C and 900°C was analyzed overall, 300°C – 400°C band in detail.

According to the DTA results, polymerization specifically starts at 245°C followed by the pyrolysis at 320°C. The latter is completed approximately around 350°C. In addition, the Curie temperature at which the phase transformation of $PbTiO_3$ takes place is measured as 490°C. Reaction time is also experimented in this study. Optimum duration for the CPP reaction is concluded as 6 hours. Lower reaction temperatures require more reaction time to complete the crystallization.

Structural changes and phase confirmations were investigated by using X-Ray powder diffraction and Raman spectroscopy. For identification, the experimental X-Ray powder data were compared and matched with the crystal database records. The particle size calculations were done by using Scherrer's equation. The particle size of the samples synthesized at 370°C turned out to be 13 nm, increasing up to 100 nm when the

heat treatment was performed at 600°C. Raman spectra allowed the investigation of the crystallinity of the samples after the annealing processes. Particularly, the soft lattice mode at 87 cm^{-1} proved to be very indicative for the state of the crystallization progress. Due to the lack of crystallization, the lattice vibration of smaller particles is less intense (softer) than that of larges ones [57]. Regarding both the XRD and Raman findings, the crystal formation develops with respect to the increasing temperature which was analyzed in related waterfall graphs.

In order to manipulate the unit cell and, thus, the ferroelectrical properties of $PbTiO_3$, the compound was doped with 0,025 mole % Fe^{3+}. $PbTiO_3$ has a distorted perovskite structure with the large lead cations on the corners; smaller titanium cation at the center and oxygens on the faces. Additional iron atoms, having lower valancy than substituted titanium atoms, act as acceptor dopants and generates a *hard* compound. Predominantly, charge compensation is achieved by the creation of oxygen vacancies ($V_O^{\bullet\bullet}$) [38]. Figure 5.1 schematizes the difference between the undoped and doped microstructural $PbTiO_3$ unit cell configuration.

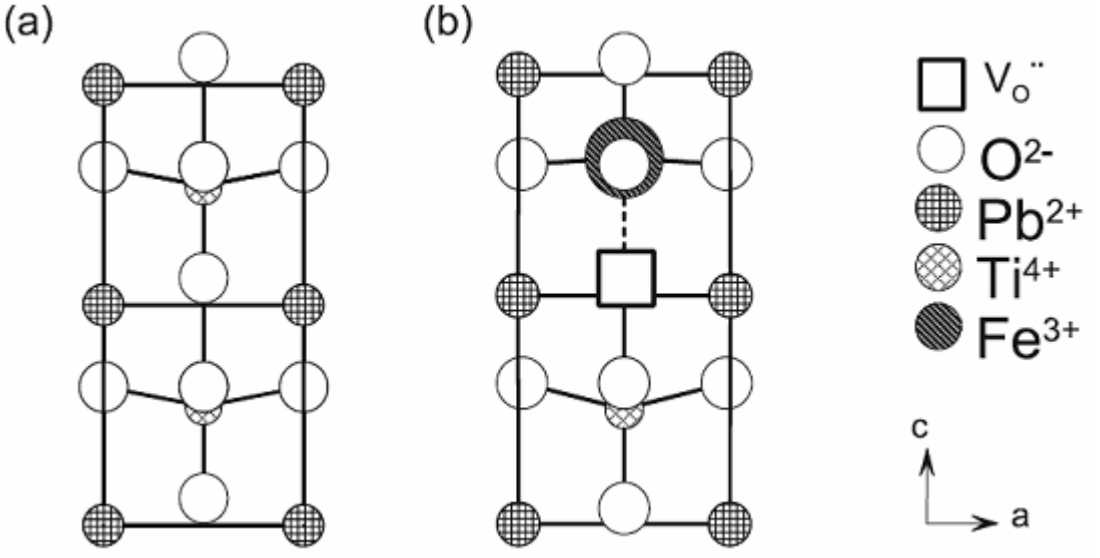

Figure 5.1 Microstructural $PbTiO_3$ unit cell configuration. a) undoped b) Fe^{3+} doped

The prevailing defect structure has been investigated by means of electron paramagnetic resonance (EPR) spectroscopy. Since undoped $PbTiO_3$ is diamagnetic, it

does not give any EPR information. However, the paramagnetic iron dopant enables EPR characterization. Thus, compound was doped with EPR active iron atoms to be able to track the changes in unit cell in response to the experimental manipulations.

Theory of size driven transitions is highly discussed issue in order to explain the order – disorder of ferroelectrics and phase transitions. The transition takes place at a certain temperature T_c(L) as the temperature varied or at a certain size L_c(T) as the particle size varied. On nanocrystalline perovskites, the transition temperature is suppressed as the sample size is reduced, and vanishes below a certain size, known as the critical size, d_{crit} [58]. The EPR results indicate marked size effects by approaching to the critical grain size $d_{crit} < 12$ nm, at which a size-driven tetragonal-to-cubic phase transition is observed at room temperature. As a function of mean grain size, either defect dipoles or "isolated" defects are formed. The obtained results agreed well with the proposed core-shell model [59, 60] and were a superposition of three phases corresponding to a ferroelectric core (tetragonal), a distorted interface layer (rhombic) and a paraelectric shell (cubic). The Fe^{3+}- modified $PbTiO_3$ nanoparticles, consisting ferroelectric core and a cubic dead layer is paraelectric. These results were also consistent with the recent Landau phenomenological theory calculations for confined ferroelectric nanoparticles [61].

In additional experiments, nanopowders were ball-milled to manipulate the unit cell and forcing the transformation from tetragonal to cubic phase. The main principle of the ball milling is based on the collision kinetics of the moving parts and the sample. Ball milling process having different durations is applied to selected samples. Most of the ball-milled samples were synthesized at relatively lower reaction temperatures, thus, characterization by using XRD and Raman did fail in most of the cases, while EPR spectra were able to show the effect of ball-milling and with respect to the milling durations.

In conclusion, it is shown that reduction in particle size down to critical size, d_{crit}, changes the structural properties of the ferroelectric $PbTiO_3$. In order to prepare nanoscale $PbTiO_3$ metal oxides, combined polymerization and pyrolysis route is an advantageous alternative synthesis route in addition to the conventional methods. Dopant usage generating defects might enhance the compounds properties, especially in dipolar

ferroelectrics compounds. Different experimental trials done in different reaction temperatures, reaction times, applying ball-milling at different durations and characterizing the yields in several methods generate better understanding of the study from a wider perspective of analysis.

Bibliography

1 R.W. Davidge, *Mechanical behavior of Ceramics*. edt. R.W. Cahn, M.W. Thompson and I. M. Ward, 1979, Cambridge University Press

2 R.W. Siegel, *Nanophase Materials*, Encyclopedia of Applied Physics, 1994, 11, VCH Publishers

3 Holler, F. James; Skoog, Douglas A; Crouch, Stanley R, "Chapter 1". *Principles of Instrumental Analysis* (6th Edition), 2007, Cengage Learning, p 9

4 Retrieved from: http://www.bostonpiezooptics.com/?D=6 on 11.11.2008

5 T. R. Narayanan Kutty, P. Padmini, *J. Mater. Chem.* 1997, 7 (3): p. 521-526

6 Retrieved from: http://materials.globalspec.com/Specifications/Materials_Chemicals_Adhesives/Ceramics_Glass_Materials/Electroceramics/Piezoelectric_Ceramic on 16.12.2008

7 Material Safety Data Sheet

8 Retrieved from: http://en.wikipedia.org/wiki/Piezoelectricity#cite_note-InstrumentAnalysis-0 on 11.11.2008

9 E. Erdem, R. Böttcher, *J. of Mater. Science*, 2003, 38: p. 3211-3217

10 L. L. Hench and L. K. West, *Principles of Electronic Ceramics*, John Wiley & Sons, Inc., 1990: p. 244-247.

11 Goldschmidt, V. M., *"Skrifter Norske Videnskaps-Akad,"* Oslo, I: Mat. - Naturv. Kl., 2,8 (1926).

12 P.M. Woodward, *Acta. Cryst.*1997, B53: p. 32-43

13 M. Johnsson and P. Lemmens, *Crystallography and Chemistry of Perovskites*, "Handbook of Magnetism and Advanced Magnetic Media",Ed. H. Kronmüller, 2006, John Wiley & Sons, New York

14 M. Lines & A. *Glass Principles and applications of ferroelectrics and related materials.* 1979, Clarendon Press, Oxford

15 "ferroelectricity." *Encyclopædia Britannica*. 2008. Encyclopædia Britannica Online. 16 Dec. 2008

16 Retrieved from: http://www.fujitsu.com/img/MICRO/fme/microelectronics/fram/ferroelectric_material.jpg

17 M. Yoshimura, K. Byrappa, *J. Mater. Sci.* 2008, 43: p. 2085-2103

18 E.K. Akdogan, A. Safari, *Ultrasonics, Ferroelectrics and Frequency Control*, 2000, 47 (4): p. 881-885

19 E. Erdem, R. Böttcher, H. Semmelhack, H. Gläsel, E. Hartmann, *Phys. Stat. Sol* 2003, 239 (2): R7-R9

20 Anthony R. West, *Chapter 2 of Solid state chemistry and its applications*, 2003, John Wiley & Sons

21 K. Byrappa, M. Yoshimura, *Handbook of Hydrothermal Technology*. 2001, Noyes Publications, NJ USA

22 K. Byrappa, *(ed) Hydrothermal growth of crystals.* 1990 Prog Cryst Grow Charact 21

23 S. Sato, T. Murakata, H. Yanagi, F. Miyasaka, *J. Mater. Sci.* 1994, 94: p. 5657-5663

24 W. Xu, L. Zheng, C. Lin, *Philosophical Maganize B*, 1998, 77 (1): p. 177-185

25 L.L.Hench, J.K.West, *The Sol-Gel Process Chem. Rev.* 1990, 90: p. 33-72
26 D. Bersani, P. Lottici, *J. of Sol-Gel Sci. and Tech.* 1998, 13: p. 849-853
27 Zavalij, V.K.P.a.P.Y., *Fundamentals of Powder Diffraction and Structural Characterization of Materials*. 2005, Springer: New York. p. 713.
28 Zavalij, V.K.P.a.P.Y., *Fundamentals of Powder Diffraction and Structural Characterization of Materials*. 2005, Springer: New York. p. 713.
29 C.A.Taylor, *A Non-Mathematical Introduction to X-Ray Crystallography*. Crystallographic Teaching. Vol. 1. 2001: Intl. Union of Crystallography. 1-10
30 Ron Jenkins, R.L.S., *Introduction to X-ray powder diffractometry.* 1996.
31 Jr W. D. Callister, Materials Science and Engineering : An Introduction. 2003, New York: Wiley.
32 Inorganic Crystal Structure Database(ICSD). 2005, FIZ Karlsruhe: Germany.
33 Stoe WINXPOW 1.2 2000, Stoe & Cie GmbH: Darmstadt
34 Ron Jenkins, R.L.S., Introduction to X-ray powder diffractometry. 1996.
35 H.P. Klug, L.E.A., X-Ray Diffraction Procedures,. 1974.
36 Bruker, *RFS 100 User Manual*. 2004.
37 K. Nakamoto, Infrared and Raman spectra of inorganic and coordination compounds 5th ed. Vol.2. 1997. New York Wiley.
38 Eichel, R. A., J. *Electroceram*, 2007 , 19: p9-21.
39 Retrieved from: http://en.wikipedia.org/wiki/Electron_spin_resonance on 12.12.2009
40 F.Speyer, R., *Thermal Analysis of Materials*. Materials Engineering, 5. *1994*: Marcel Dekker,Inc. 285.
41 E. Erdem, R. Böttcher, H. -C. Semmelhack, H. -J. Gläsel, E. Hartmann, D. Hirsch, *J. Mater. Sci*. 38, 2003, 3211.
42 E. Erdem, H.C. Semmelhack, R. Böttcher H. Rumpf, J. Banys, A. Matthes, H. -J. Gläsel, D. Hirsch, E. Hartmann, *J. Phys. Cond. Mat*. 18, 2006, 3861.
43 R. Böttcher, C. Klimm, D. Michel, H. -C. Semmelhack, G. Völkel, H. -J. Gläsel, E. Hartmann, *Phys. Rev*. B 62, 2000, 2085.
44 E. Erdem, A. Matthes, R. Böttcher, H.-J. Gläsel, and E. Hartmann, *J. Nanosciences and Nanotechnology* 8, 2008, 702.
45 G.I. Dzardimalieva, A.S. Rozenberg, A.D. Pomagailo, *Russ. Chem. Bull*. 44, 1995, 858.
46 Glazer, A.M., Mabud, S.A., Acta Crystallogr., Sec. B, 34, (1978), 1065
47 G. Burns and B. A. Scott, *Phys. Rev.* B 7, 1973, 3088.
48 Ishikawa K, Nomura T, Okada N and Takada K 1996 *Japan. J. Appl. Phys.*
49 Erdem, E. et.al J. Phys.: *Condens. Matter* 18, 2006, 3861–3874
50 R.-A. Eichel, H. Mestric, K.-P. Dinse, A. Ozarowski, J. van Tol, L.C. Brunel, H. Kungl, M.J. Hoffmann, *Magn. Reson. Chem*. 43, 2005, S166.
51 P. Erhart, R.-A. Eichel, P. Traskelin, K. Albe, *Phys. Rev*. B 76, 2007, 174116.
52 R.-A. Eichel, P. Erhart, P. Traskelin, K. Albe, H. Kungl, M.J. Hoffmann, *Phys. Rev. Lett.* 100, 2008
53 H. Mestric, R.-A. Eichel, T. Kloss, K.-P. Dinse, So. Laubach, St. Laubach, P.C. Schmidt, *Phys. Rev.* B 71, 2005

54 E. Erdem, R.-A. Eichel, H. Kungl, M.J. Hoffmann, A. Ozarowski, H. van Tol, L.C. Brunel, IEEE-TUFFC 55, 2008
55 E. Erdem, M.D. Drahus, R.-A. Eichel, H. Kungl, M.J. Hoffmann, A. Ozarowski, H. van Tol, L.C. Brunel, *Funct. Mat. Lett.* 1, 2008
56 E. Erdem, R.-A. Eichel, H. Kungl, M.J. Hoffmann, A. Ozarowski, H. van Tol, L.C. Brunel, *Phys. Scr.* T129, 2007
57 K. Ishikawa, K. Yoshikawa, N. Okada, *Phys. Rev. B*, 37, 10, 1988
58 K. Sheshadri, R. Lahiri, P. Ayyub, S. Bhattacharya, *J. Phys. Cond. Mat.* 11, 1999
59 E. Erdem, H.C. Semmelhack, R. Bottcher H. Rumpf, J. Banys, A. Matthes, H. -J. Glasel, D. Hirsch, E. Hartmann, *J. Phys. Cond. Mat*. 18, 2006
60 S. Aoyagi , Y. Kuroiwa, A. Sawada, H. Kawaji, T. Atake, *Journal Thermal Analy. Cal.*, 81, 2005, 627.
61 A. N. Morozovska, M. D. Glinchuk, E. A. Eliseev, *Phys. Rev. B* 76, 2007

Vita

Kamil Kiraz was born in Balıkesir, Turkey, in 1983. He completed high school in Balıkesir Sırrı Yırcalı Anadolu Lisesi in 2001. He received his B.S. degree in Chemistry from KoçUniversity, İstanbul – Turkey, in 2006. The same year, he started his Master studies in the program Material Science and Engineering at Koç University. He will continue his academic career in a PhD program in Technical University of Eindhoven – Netherlands. Hydrogen storage of magnesium alloys will be the next topic of his studies.